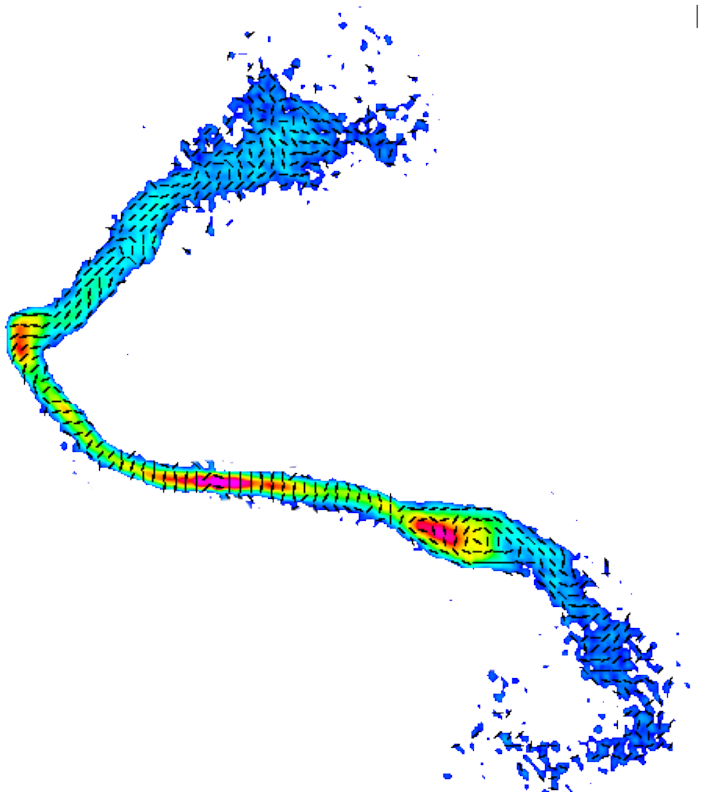

Polarimetry of a Giant Radio Galaxy

A polarization analysis of the Double Irony giant radio galaxy in the 4-8 GHz range

Master's thesis in Physics

DANIEL PERSSON ILONEN

DEPARTMENT OF SPACE, EARTH AND ENVIRONMENT

CHALMERS UNIVERSITY OF TECHNOLOGY
Gothenburg, Sweden 2022
www.chalmers.se

Master's thesis 2022

Polarimetry of a Giant Radio Galaxy

A polarization analysis of the Double Irony giant radio galaxy in the 4-8 GHz range

Daniel Persson Ilonen

CHALMERS
UNIVERSITY OF TECHNOLOGY

Department of Space, Earth and Environment
Division of Astronomy and Plasma Physics
Onsala Space Observatory
Chalmers University of Technology
Gothenburg, Sweden 2022

Polarimetry of a Giant Radio Galaxy
A polarization analysis of the Double Irony giant radio galaxy in the 4-8 GHz range
Daniel Persson Ilonen

© DANIEL PERSSON ILONEN, 2022.

Supervisor: Prof. Cathy Horellou, Department of Space, Earth and Environment
Examiner: Prof. Cathy Horellou, Department of Space, Earth and Environment

Master's Thesis 2022
Department of Space, Earth and Environment
Division of Astronomy and Plasma Physics
Chalmers University of Technology
SE-412 96 Gothenburg
Telephone +46 31 772 1000

Onsala Space Observatory
SE-439 92 Onsala
Telephone +46 31 772 5500

Cover: Intensity map of the Double Irony galaxy imaged in C-band, showing the Stokes I continuum intensity. Overlaid vectors show linear polarisation angle with an offset of 90 degrees to visualise the magnetic field.

Typeset in LaTeX
Printed by Chalmers Reproservice
Gothenburg, Sweden 2022

Polarimetry of a Giant Radio Galaxy
A polarization analysis of the Double Irony radio galaxy in the 4-8 GHz range
DANIEL PERSSON ILONEN
Department of Space, Earth and Environment
Chalmers University of Technology

Abstract

Radio galaxies can display jets and lobes of radio emission from an active galactic nucleus located at the center of their host galaxy. These jets and lobes extend well beyond the host galaxy. The radio structures are valuable probes of the environment of the galaxies into which they expand. Polarimetry provides additional information of the magneto-ionic medium in and around radio galaxies.

New observational data of synchrotron emission from the Giant Radio Galaxy named Double Irony were imaged and analysed. The radio galaxy extends about 1100 kiloparsec in length and lies at a redshift of 0.138. This observation was made by the Jansky Very Large Array interferometer in the 4.2 to 8.2 GHz frequency range, with a 2 MHz spectral resolution. The Stokes I data were calibrated using a calibration pipeline. Polarimetry data were manually calibrated using the output of the calibration pipeline as a starting point.

Wideband Stokes I continuum was first imaged. The resulting images have a higher angular resolution than previous works with a synthesised beam of $3.36'' \times 2.65''$, or 8.21×6.47 kiloparsec. After primary beam attenuation correction the spectral index map was calculated, using both wideband images and individual frequency bands of 128 MHz.

Using Rotation Measure Synthesis, the Stokes Q and Stokes U wideband data were corrected for Rotation Measure. Linear polarisation intensity and linear polarisation angles were obtained, and the magnetic field distribution in the different structures of Double Irony was calculated. The polarimetry data show signs of helical magnetic fields with toroidal magnetic field components around certain parts of the jets.

Keywords: Double Irony, Giant Radio Galaxy, Polarimetry, Polarization, Faraday Rotation, Rotation Measure, VLA, Very Large Array, Interferometry.

Acknowledgements

I would like to extend my deepest gratitude to my supervisor, Prof. Cathy Horellou. This thesis would not have been possible without her unending enthusiasm for both radio astronomy and for her students. I am also grateful to the NRAO staff and lecturers at the 8th VLA Data Reduction Workshop, for organising the workshop and for helping me understand the VLA dataset and the calibration process. Many thanks to Mark Birkinshaw for his interest in the project and his expert advice on the data analysis.

I would also like to thank my closest family, my father and my sister, for their steadfast support during this period, and for always encouraging my endeavours. Special thanks to my girlfriend for her patience with me during the writing of this thesis.

Daniel Persson Ilonen, Gothenburg, August 2022

Contents

List of Figures

List of Tables

1

Introduction

1.1 The XXL Survey and Double Irony

The XXL Survey was a multiwavelength survey covering 50 deg^2 of the sky. The X-ray part of the survey, carried out with the XMM-Newton satellite, consists of over 500 observations. These observations covered two 25 deg^2 patches of the sky, named XXL-north and XXL-south. The main scientific motivation of this study as described in Pierre et al. (2016) was to provide a sample of galaxy clusters suitable for cosmology studies, and a large sample of Active Galatic Nuclei (AGN) for studies of galaxy evolution. The XXL survey was conducted mainly in the X-ray frequency band, or in the 0.5 to 2 keV range (Pierre et al., 2017), while also being complemented by several multiwavelength observations in the XXL survey areas (Pierre et al., 2016). The focus of this thesis is a particularly large radio galaxy discovered in the radio survey of the XXL-North field carried out by Smolčić et al. (2018), named the Double Irony (Horellou et al., 2018).

According to previous observations, the Double Irony galaxy features structures that extends over a distance of 1100 kpc, classifying it as a giant radio galaxy. The central host galaxy has been identified to lie at a redshift of $z = 0.1375$ with a stellar mass of $\sim 3 \times 10^{11} M_{\odot}$ (Horellou et al., 2018). From this central point we observe several distinct features, marked and labeled in figure 1.1. From the central core we can observe two jets, culminating in areas with higher flux density, namely the ”Elbow” to the east and the ”SW1” area in the south-west. From these areas two diffuse-like structures stretch to the north marked ”N” and to the south-west marked ”SW2”. Naming of the regions is taken from previous literature on the subject (Horellou et al., 2018). The distinct shape of these features in the form of two inverted question marks have given rise to the name "Double Irony".

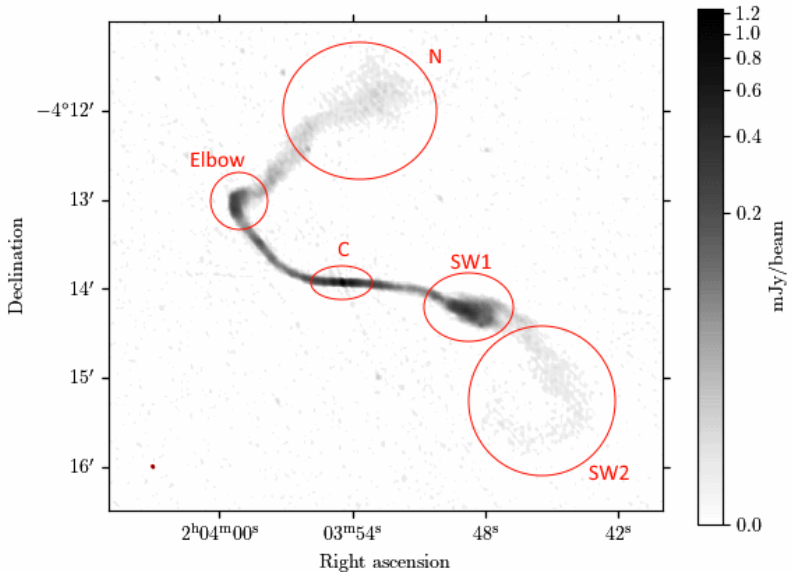

Figure 1.1: The Double Irony giant radio galaxy Stokes I continuum at 4-8 GHz, with named regions marked in red. Naming of regions taken from Horellou et al. (2018).

In 2018 an analysis of this galaxy was made in the 610 MHz and 1.4 MHz range from the Giant Meterwave Radio Telescope (GMRT) and VLA respectively (Horellou et al., 2018). In 2019 further work was done using VLA data in the 2-4 GHz range, including polarimetry (Montoya Arroyave, 2019).

1.2 Thesis Scope and Outline

The aim of this thesis is to analyse new observational data that were obtained in 2020 of the Double Irony Galaxy. These data were collected by the VLA interferometer in the 4.2-8.2 GHz range (C-band). The newly obtained data provide a higher angular resolution than previous data that exist in the 1-2 GHz and 2-4 GHz range. This thesis covers the Stokes I wideband continuum as well as polarisation data, and aims to compare these new results with previous analyses in the lower frequency range.

Data calibration and imaging in this thesis was done mostly using the CASA 6.1 software. For stokes I continuum calibration the VLA pipeline was used, while for polarisation the data were calibrated manually. The scope of the thesis will also cover image cleaning algorithms and imaging results for both continuum and polarisation data. Using polarisation data the magnetic field lines projected in the plane of the sky and the degree of polarization of the observed synchrotron radiation can be determined. Finally the foreground Faraday rotation will also be analysed and compensated for using rotation measure synthesis.

Chapter 1 is an introduction to the subject and outline of the thesis. Chapter 2 will be a description of interferometry basics, based on the VLA, together with a basic

explanation of synchrotron radiation and polarimetry. In Chapter 3 the raw data collection during the VLA observation is discussed, along with calibrators and the calibration processes used. This chapter also contains a description of imagining techniques used in the CASA software. Chapter 4 will present the final images in Stokes I continuum, spectral index, Stokes Q, U and V, Rotation Measure Synthesis results, fractional polarisation and linear polarisation angle. In Chapter 5 final remarks and future suggestions will be presented.

2

Theory

2.1 Interferometry

An interferometer effectively uses multiple antennas to synthesise an aperture with a diameter comparable to longest distance between two antennas. The antennas measure the interference pattern created by constructive and destructive self-interference from the source. For a more formal description, we consider the 2D projected distribution of antennas on a spatial plane (x, y) seen from an astronomical source at some declination. We then define the collection of baseline vectors as all vectors between unique antenna positions, such that for n antennas there are $n(n-1)/2$ baselines. The baselines are placed on a plane (u, v) in spatial frequency space such that the relative angles are retained, but the each baseline vector has its origin at the origin of the (u, v) plane. Finally the (u, v) plane for the interferometer is described by the collection of points in the (u, v) plane that describes the endpoints of each vector. See figure 2.1 for an example of VLA (x, y) and (u, v) planes.

Over time, the individual data points in the (u, v) plane of a given baseline are distributed along part of an ellipse on the (u, v) plane due to the rotation of the earth, where the shape depends on the declination of the source and the total observation time. The coverage in the (u, v) plane represents the points where we can sample data in the synthesised aperture, and affects how well the source can be imaged.

The raw visibility data, $V_{obs}(u, v)$, collected from an interferometer is the Fourier transform of the intensity distribution of the source $I_{sky}(x, y)$ discretely sampled at points $S(u, v)$, as created by the baselines of the interferometer, via

$$V_{obs}(u, v) = \mathcal{F}[I_{sky}(x, y)] \cdot S(u, v). \tag{2.1}$$

Alternatively one can describe the intensity collected as a convolution between the interferometer point spread function, $I_{psf}(x, y) = \mathcal{F}^{-1}[S(u, v)]$, and the source intensity $I_{sky}(x, y)$ such that

$$I_{obs}(x, y) = I_{sky}(x, y) * I_{psf}(x, y). \tag{2.2}$$

To get any useful images, and the actual sky brightness distribution, from the collected visibility data V_{obs} we then need to inverse Fourier transform the visibilities and deconvolve the resulting image from the PSF.

2.1.1 The Very Large Array Interferometer

The data analysed in this project were collected using the *Karl G. Jansky Very Large Array* Interferometer, often abbreviated VLA, or JVLA. The VLA is located in New Mexico, USA, in the northern hemisphere at a latitude of approximately 34°, and is a facility operated by the National Radio Astronomy Observatory organisation, NRAO. The interferometer consists of 27 antennas, each with a dish size of 25m, positioned in an inverted Y-pattern (NRAO Telescopes, n.d.).

The VLA interferometer is special in the regard that the individual antennas can be moved further apart for higher spatial resolution, or closer together for resolving structures. There are four configurations, named A B C and D. The configurations only differ in where along the three arms the antennas are placed. In the smallest configuration the antennas have a maximum baseline of 1.03 km, while the most spread out configuration results in a maximum baseline of 36.4 km. An example of an array configuration (the A-configuration, or the the most extended configuration), is shown in fig. 2.1.

This Y-pattern tends to result in, depending on observation time and source declination, a well covered (u, v) plane. See fig. 2.1 for the typical snapshot (u, v) coverage of an overhead source in the A configuration.

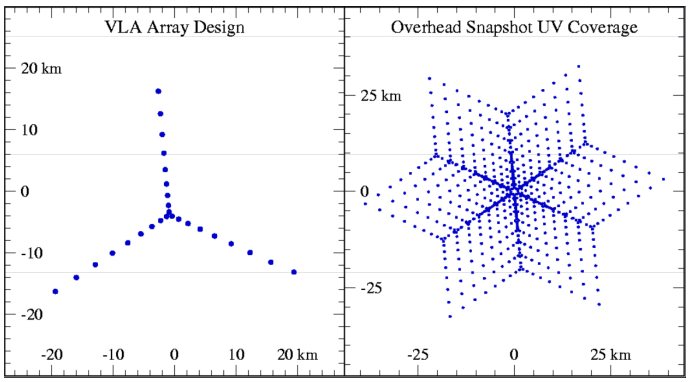

Figure 2.1: Left: VLA antenna distribution in A configuration. Right: (u, v) coverage snapshot (Mioduszewski, 2010).

Depending on the array configuration and observed frequency there are limits on the largest angular scale θ_{LAS} that can be imaged, as well as the angular resolution, or synthesised beamwidth, θ_{HPBW}. Fig. 2.2 gives an estimate of the angular resolution of each array configuration plotted versus frequency.

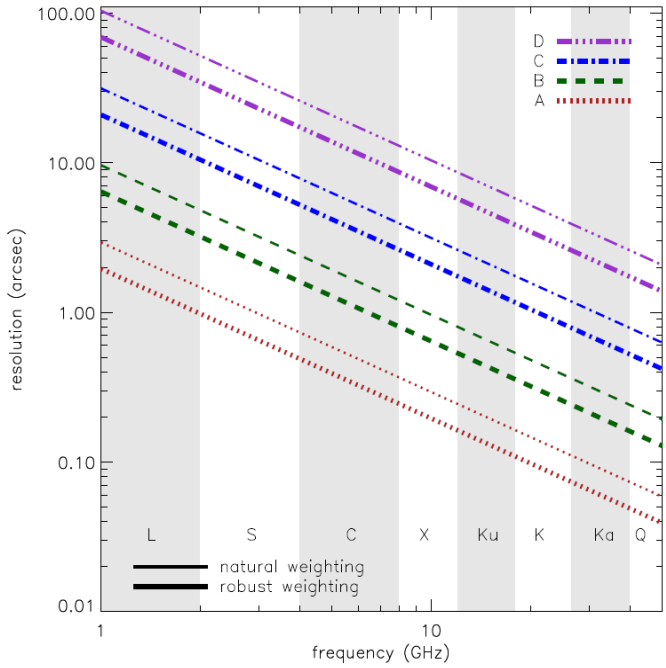

Figure 2.2: Log-log plot of VLA estimated synthesised beamwidth θ_{HPBW} versus frequency for the different array configurations and for different weightings of the (u, v) data (see chapter 2.4.1 for more information on weightings). (VLA Manuals, n.d.)

2.2 Synchrotron Radiation

Synchrotron radiation is the dominant radio emission mechanism that we observe from structures around active galactic nuclei in sub 30GHz frequencies (Condon and Ransom, 2016). A single charged particle undergoing acceleration produces electromagnetic radiation with total power P according to Larmor's Formula:

$$P = \frac{2q^2\dot{v}^2}{3c^3} \tag{2.3}$$

If this particle is accelerated by an magnetic field, magnetobremsstrahlung is produced. Furthermore the characteristics of the magnetobremsstrahlung is dependent on the speed of the charged particle. If the particle is an ultrarelativistic electron with kinetic energies $\gg m_e c^2$ the radiation is called synchrotron radiation.

If we consider this ultrarelativistic electron to be moving in a homogeneous magnetic field $\mathbf{B}$ with velocity $\mathbf{V}$ the motion of this electron is described by

$$\frac{d}{dt}\gamma m_e \mathbf{V} = \frac{e}{c}(\mathbf{V} \times \mathbf{B}) \tag{2.4}$$

(Wilson et al., 2013) where γ is the velocity dependent relativistic Lorentz factor of the electron. Using the energy-momentum relationship we state the particle energy

as $E = \gamma m_e c^2$. Since the energy of the particle remains constant in the absence of an external electric field we add the constraint

$$\frac{d}{dt}(\gamma m_e c^2) = 0. \tag{2.5}$$

This relationship implies

$$\frac{d}{dt}\gamma = 0 \implies |\mathbf{V}| = const. \tag{2.6}$$

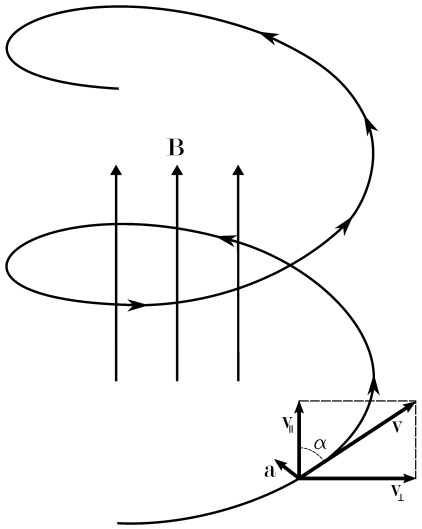

Figure 2.3: Motion of charged particle in homogeneous magnetic field **B** with particle velocity **v** and pitch angle α

Separating $|V|$ into $v_\parallel$ parallel to **B** and $v_\perp$ perpendicular to **B** according to figure 2.3 we can see the following relationships:

$$\frac{d}{dt}v_\parallel = 0, \tag{2.7}$$

$$\frac{d}{dt}v_\perp = \frac{e}{\gamma m_e c}(v_\perp \times \mathbf{B}). \tag{2.8}$$

From equation 2.7 and 2.6 follows that $|v_\perp|$ is also constant. Thus the velocities describe a uniform circular motion with a gyration frequency of

$$\omega_B = \frac{eB}{\gamma m_e c} \tag{2.9}$$

(Rybicki and Lightman, 1979).

We see in figure 2.3 that the acceleration of the particle will be in a plane normal to the magnetic field **B**, and we denote this acceleration as $a'_\perp$ in the inertial frame of

the electron at rest. In the frame of an observer at rest in the source of the radiation, i.e. moving with velocity V relative to the electron, we denote the acceleration of the electron as $a'_\perp = a_\perp/\gamma$. Inserting this in the Larmor's equation (2.3) we get the radiated power of a single ultrarelativistic electron as

$$P = P' = \frac{2e^2 a_\perp^2 \gamma^4}{3c^3} \tag{2.10}$$

with the $P = P'$ relationship stemming from power being a relativistic invariant.

From the relationship $a_\perp \equiv \omega_B v_\perp$ we can write equation 2.10 in terms of pitch angle α (fig. 2.3) as

$$P = \frac{2e^2}{ec^3}\gamma^2 \frac{e^2 B^2}{m_e^2 c^2} v^2 \sin^2 \alpha. \tag{2.11}$$

Another important feature of synchrotron radiation is the so called relativistic aberration, or beaming. A detailed description, using relativistic velocity addition, can be found in Condon and Ransom (2016). Due to the relativistic speed of the electron and the helical path it travels on, an observer at rest will see synchrotron radiation as confined to a narrow beam. This beam will have an angular width of $\phi = 2/\gamma$ as per fig. 2.4.

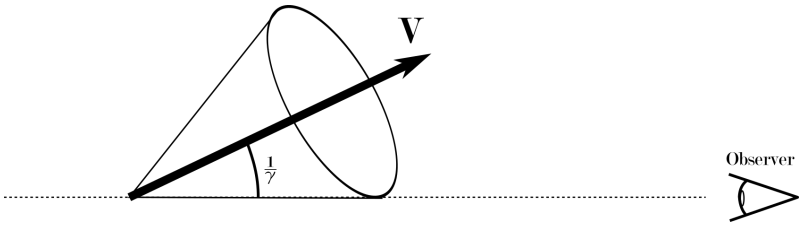

Figure 2.4: Beaming of synchrotron radiation from ultrarelativistic electron moving with velocity **V**.

As the electron travels along a helical path the emission cone will sweep the observer as a series of narrow pulses with a duration of

$$\Delta t_p = \frac{\phi \omega_b}{2\gamma^2} \frac{1}{\sin \alpha} = \frac{1}{\gamma^3 \omega_B} \frac{1}{\sin \alpha} \tag{2.12}$$

with a time between pulses of

$$\Delta t = \frac{\gamma}{\nu_{gyration}} = \frac{2\pi}{\omega_B} \tag{2.13}$$

where $\Delta t \gg \Delta t_p$. The synchrotron spectrum from a single electron is the Fourier transform of these pulses (Condon and Ransom, 2016).

2.2.1 Spectral Index

We can now look at the synchrotron spectrum of an ensemble of electrons with different velocities and pitch angles, which is what we are observing in a real world scenario.

We begin by defining the spectral index as α in the power law

$$S(\nu) \propto \nu^{\alpha} \tag{2.14}$$

where $S(\nu)$ is the frequency dependent observed flux density.

We can describe the power spectrum of an optically thin source of synchrotron radiation as a superposition of individual spectra from electrons. The energy distribution of these electrons following a power law as

$$n(E)dE \propto E^{\delta}dE \tag{2.15}$$

where $n(E)dE$ is the density of electrons between energies $E + dE$. The spectral index α is related to the exponent δ of the electron energy distribution by

$$\alpha = \frac{\delta - 1}{2}. \tag{2.16}$$

The power radiated by each electron with gyration frequency ν_B peaks at a critical frequency $\nu_c \approx \gamma^2 \nu_B$. As the electron travels farther and radiates energy E with time, the critical frequency decreases. The energy loss due to synchtrotron radiation is proportional to E^2, and the higher energy electrons are depleted first. Since the aforementioned power laws are the sum of individual electron power spectra we can expect areas of older electrons to have steeper spectral index due to these radiation energy losses, if no new energy is injected (Pacholczyk, 1970).

2.3 Polarimetry

An important feature of synchrotron radiation is that it is polarised. The degree of polarisation is related to the magnetic field in the source (Thompson et al., 2017).

An electromagnetic wave $\vec{E}$ propagating in $\hat{z}$ can be described as components projected orthogonally as

$$\vec{E} = [\hat{x}E_x e^{i\phi_x} + \hat{y}E_y e^{i\phi_y}]e^{i(\vec{k}\cdot\vec{z}-\omega t)} \tag{2.17}$$

where $\vec{k}$ is the wave vector and ω the angular frequency.

We also define $\varphi = \phi_x - \phi_y$ as the phase difference between E_x and E_y.

Linearly polarised light would result in $\varphi = 0$. Circularly polarised light is described by a phase of $\pi/2$ and $E_y = E_x$. Both cases are special cases of elliptical polarisation.

2.3.1 Stokes Parameters

The four Stokes parameters characterize the average polarisation over timescales $t \gg (\Delta\omega)^{-1}$ for the frequency range $\Delta\nu = \Delta\omega/2\pi$.

$$I =< E_x^2 + E_y^2 > /R_0 \tag{2.18}$$

$$Q =< E_x^2 - E_y^2 > /R_0 \tag{2.19}$$

$$U =< 2E_x E_y \cos(\varphi) > /R_0 \tag{2.20}$$

$$V =< 2E_x E_y \sin(\varphi) > /R_0. \tag{2.21}$$

I describes the total flux density and R_0 the radiation resistance of free space [1] as per the convention of Condon and Ransom (2016). Stokes parameters Q and U represents the linearly polarised component, while V describes the circularly polarized component. We expect I to be always positive, while Q, U and V can take negative or positive values depending on the polarisation (Thompson et al., 2017).

The degree of polarisation is defined as

$$p = \frac{\sqrt{Q^2 + U^2 + V^2}}{I} = \frac{I_{polarized}}{I_{total}}. \tag{2.22}$$

The linearly polarized component of the flux density is defined simply by $\sqrt{Q^2 + U^2}$, since the V component represents circular polarisation. Using the Stokes parameters Q and U, we can define the linear polarisation angle as

$$\chi = \frac{1}{2}\tan^{-1}\left(\frac{U}{Q}\right), \quad 0 \leq \chi \leq \pi \tag{2.23}$$

2.3.2 Faraday Rotation and Rotation Measure

If we assume the electrons creating the synchrotron radiation to have isotropically distributed velocities and follow the power law distribution in equation 2.15, then we can expect the degree of polarization (equation 2.22) to follow

$$p(\delta) = \frac{3\delta - 3}{3\delta - 7} = \frac{3\alpha - 3}{3\alpha - 5}. \tag{2.24}$$

independent of frequency (Le Roux, 1961)[2], (Brentjens and de Bruyn, 2005). However in real observations we see polarisation fractions of much lower values. Burn (1966) showed that random fluctuations of the magnetic field in the source is one factor which can decrease the polarisation intensity. The magnitude of this effect can be shown to be $p = p(\delta) \times \frac{E_{uniform\ field}}{E_{total\ field}}$

[1] $R_0 = 4.19 \times 10^{-10}$ cm^{-1} s in CGS units, or 377 Ω in MKS units

[2] Note that the sign of δ and α used in the power laws differs in the literature, and the convention used in this thesis is different from that in most papers cited in this section.

Another depolarizing mechanism is Faraday dispersion. Between the source of synchrotron radiation and the observer we have the interstellar medium, ISM, and also possibly the intergalactic medium, containing free electrons. In this intervening medium we might also find magnetic fields with some portion of the field being parallel to the direction of travel of the electromagnetic waves from the source. Around this parallel magnetic field the free electrons of the ISM are gyrating with some angular frequency $\omega_G = \frac{eB}{m_e C}$. Depending on the magnetic field strength, gyration frequency in the foreground medium, and on the polarisation direction of the incident wave, the refraction index in the foreground medium plasma will differ. More specifically the refractive index is dependent on the conductivity, $\sigma \propto (\omega \pm \omega_G)^{-1}$, where ω is the angular frequency of the incoming wave, and the sign in $\pm\omega_G$ depends on left or right hand polarisation (Condon and Ransom, 2016).

The incident linearly polarised electromagnetic wave traveling through this medium is a superposition of right- and left- hand circularly polarised waves. Since one of the factors affecting the refraction is the direction of polarisation, the right hand polarised component will travel with a different speed through the medium than the left hand polarised component. This will cause the angle of polarisation to change, as seen in figure 2.5.

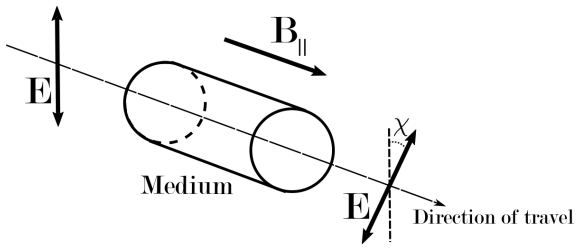

Figure 2.5: Faraday rotation of linearly polarised light through a magneto-ionic medium.

Rotation measure is the change in polarization position angle along a distance. This is wavelength dependent such that the change $\Delta\chi = \lambda^2 RM$, where RM is the Rotation Measure, or the amount of rotation given in rad m^{-2}. The Rotation Measure is related to the integral of the product of the density of thermal electrons, n_e, and the parallel component of the magnetic field along the line of sight, $B_\parallel$, as

$$RM \approx 8.1 \times 10^5 \int_{Los} n_e B_\parallel dl \quad \text{rad/m}^2 \tag{2.25}$$

given n_e in cm^{-3}, B$_\parallel$ in Gauss and distance dl in parsec along the line of sight to the source.

Using the so-called Rotation Measure Synthesis (Brentjens and de Bruyn, 2005) we can use data with a high spectral resolution over a large frequency range to calculate the RM. This provides information on the direction and magnitude of magnetic fields along the line of sight, and allows us to correct for the Faraday rotation and determine the polarisation angle of the source.

2.4 Imaging

As introduced in chapter 2.1, the observed visibility data are the discretely sampled Fourier transform of the intensity distribution of our source. To obtain useful images showing the intensity of different Stokes parameters we need to apply some imaging techniques to the data. We recall from equation 2.2 that $I_{obs} = I_{sky} * I_{psf}$, and the goal of imaging is to re-create I_{sky}. I_{obs} can also be referred to as the dirty image, while I_{psf} is sometimes referred to as the synthesised dirty beam.

2.4.1 Weighting

The simplest dirty beam used to deconvolve I_{obs} is just the inverse Fourier transform of the sampling function $S(u, v)$ (equation 2.1), which is a function of the baseline distribution of the interferometer. However we can apply a weighting to the dirty beam such as

$$I_{psf}(x, y) = \mathcal{F}^{-1}[w(u, v)S(u, v)] \tag{2.26}$$

where $w(u, v)$ is the weighting function. This weighting can be an arbitrary function and is most commonly used to change beam shape, side lobe levels, signal-to-noise ratio and dynamic range.

In real world applications the observed u, v data need to be sampled in a way where the data can be treated discretely. This is called gridding, and involves spacing the visibilities on a regular grid using interpolation. Thus we can redefine the sampling function $S(u, v)$ as

$$S(u, v) = \sum_{j=1}^{J/2} [{}^2\delta(u - u_j, v - v_j) + {}^2\delta(u + u_j, v + v_j)] \tag{2.27}$$

where (u_j, v_j) are the coordinates of sampling point j and ${}^2\delta$ is the two-dimensional Dirac function located at the sampling point (Thompson and Bracewell, 1974). J is the number of points to sample. We can now treat the weighting function $w(u, v)$ as weighting discrete points $w(u_j, v_j)$ in a regularly distributed grid as well.

A simple weighting function called 'natural weighting' works by setting weights that are inversely proportional to the noise variance, σ, of the visibilities, thus areas with high noise are weighted down. We write the natural weighting $w_{j,k}(u, v)$ at grid cell j containing visibilities k as

$$w_{j,k}^{Nat} = \frac{1}{\sigma_k^2}. \tag{2.28}$$

Natural weighting gives a good dynamic range, or maximum brightness to noise ratio, since it suppresses RMS noise. However it sacrifices angular resolution of the final image due to heavily weighting down gridded points containing the most visibilities, usually at shorter baselines.

An alternative to natural weighting is uniform weighting. Uniform weighting takes the number of visibilities per grid cell into consideration. For visibilities (u_k, v_k) in

grid cell j, uniform weighting is defined as

$$w_{j,k}^{Uni} = \frac{w_{j,k}^{Nat}}{\omega_j},\ \omega_j = \sum_{l=1}^{N_j} \frac{1}{\sigma_l^2} \tag{2.29}$$

where N_j is the number of visibilities in grid cell j. Uniform weighting results in higher angular resolution but higher RMS noise compared to natural weighting.

Finally we introduce robust weighting, or Briggs weighting, by Briggs (1995). This weighting is defined by

$$w_{j,k}^{Briggs} = \frac{w_{j,k}^{Nat}}{1 + f^2\omega_j},\ f^2 = \frac{\sum_{i=1}^{N_{vis}} w_{i,k}^{Nat}}{\sum_{i=1}^{N_{cell}} \omega_i^2}(5 \times 10^{-R})^2 \tag{2.30}$$

where N_{vis} is the total number of visibilities and N_{cell} is the total number of grid cells (CASA Toolkit Reference Manual, n.d.). The f^2 term describes the sum of natural weights for all visibilities divided by the sum of uniform weights over all grid cells for the entire image. The R exponent is the 'robust' parameter. This parameter normally takes values between -2 to 2, and modifies the Briggs weighting to lie in a continuous range between uniform weighting and natural weighting. This robust weighting can according to Briggs (1995) reduces the RMS thermal noise of a uniformly weighted VLA image by up to 25%, and allows for a high flexibility between high angular resolution and low RMS noise. This is the primary weighting used for this thesis.

2.4.2 Deconvolution Algorithms

To deconvolve the dirty beam from the true sky visibilities I_{sky}, a multitude of algorithms have been developed. This chapter will discuss the two algorithms that were used to produce the results of this thesis. The first algorithm is the ubiquitous 'CLEAN' algorithm by Högbom (1974). This is a iterative algorithm that treats the sky image as a collection of point sources on a empty background. 'CLEAN' then looks for the peak brightness in the dirty image, and defines that as the 'CLEAN' component. The dirty beam is convolved with a point source and then multiplied by some gain $\gamma \in (0, 1]$. This resulting PSF is subtracted from the image at the location of the 'CLEAN' component. The image left after subtraction is called the residual image, and the point source that was subtracted is added to the clean image. This process is repeated until the residual image brightness is below some certain threshold. Lastly the collection of point sources, or $^2\delta$-functions in the clean image are convolved with a clean Gaussian beam, and the residuals are added back into the clean image.

The Högbom 'CLEAN' algorithm was initially made for point sources but performs very well with extended sources. However when dealing with a wide frequency band for an extended source where we want to examine the spectral index, there is another algorithm that works well, the MT-MFS (Multi Term - Multi Frequency Synthesis) by Rau and Cornwell (2011). This is similar to 'CLEAN' in that it is an iterative

algorithm that produces a residual, but the modeling of the sky brightness differs. In principle this algorithm works by modeling wideband brightness distributions as inverted, tapered paraboloids on different size scales. The amplitudes of these paraboloids follow some Taylor polynomial in frequency space (CASA Documentation, n.d.). The Taylor terms can be used to determine the spectral index α and thus the frequency dependency of the sky brightness.

3

Methods

3.1 Data Collection

The data were collected the 11th of April 2020 by the VLA interferometer in its C-configuration. The interferometer had 26 active antennas out of 27, with a minimum baseline of 44.8 m and a maximum baseline of 3.4 km.

The target source was observed in the 4.22 GHz to 8.22 GHz range. The measurement data are separated into 32 spectral windows, each of a bandwidth of 128 MHz. Each individual spectral window contains 64 measurement channels at a spectral resolution of 2 MHz per channel. Due to the measurement instrument naming convention of the VLA, the spectral windows are numbered as 16 to 47. For a detailed list of observed spectral windows see Appendix table A.1.

The total observation run lasted between 19:43:40 UTC time until 23:42:55 UTC. This resulted in a total of 3 hours and 55 minutes of on source time, out of which 2 hours and 55 minutes where on the Double Irony science target source. The observation was set up such that four calibrators were observed in addition to the science target, see table 3.1. The calibrator 3C138 was targeted at the beginning and end of the observation, and the calibrators 3C84 and J0359+505 were targeted at the end of the observation. During the main part of the observation the interferometer was alternating between the phase calibrator J0157-1043 in 90 second periods, and the science target Double Irony in 555 second periods. For a complete observation schedule see fig. 3.2. The array configuration and observation time results in a (u, v) coverage visible in fig. 3.1.

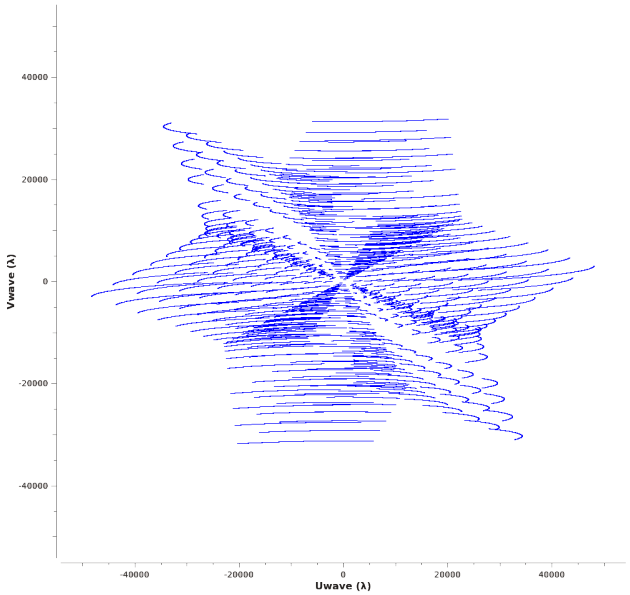

Figure 3.1: (u, v) coverage of data in spectral window 16, centred at $\nu_c = 4.29$ GHz with width $\Delta\nu = 128$ MHz.

During the observation there were some high winds, and some antennas had to be temporarily stowed into an upright position to protect them from wind damage. However this did not cause any major problems to the data. See Appendix fig. A.3 for information on each antenna's pointing error and its pointing status. In total 16.17 percent of all data was flagged due to antenna slewing when switching target and wind induced stowing.

Source	Field ID	Observation Time	Right Ascension	Declination
3C138	0	19 min 45 sec	05:21:09.88602	+16.38.22.0512
J0157-1043	1	32 min 50 sec	01:57:41.52800	-10.43.40.4080
Double Irony	2	175 min 20 sec	02:03:54.00000	-04.13.56.0000
3C 84	3	5 min 0 sec	03:19:48.15976	+41.30.42.1142
J0359+5057	4	2 min 55 sec	03:59:29.74726	+50.57.50.1615

Table 3.1: Sources with their respective assigned field ID number, cumulative observation time and J2000 coordinates.

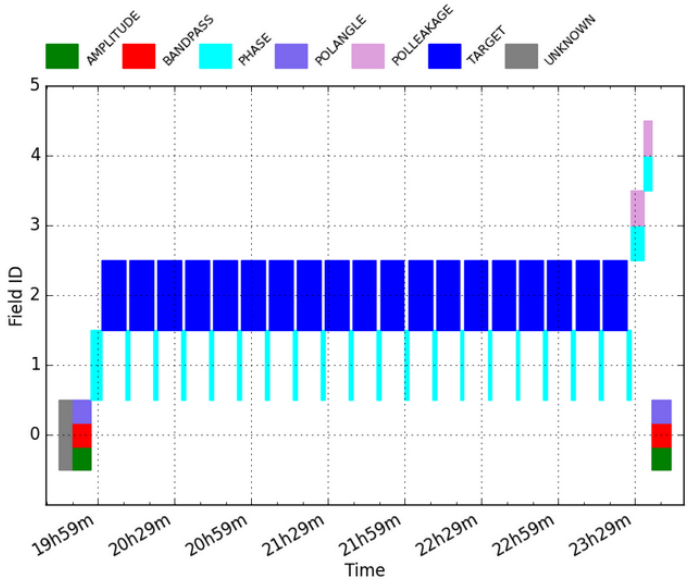

Figure 3.2: Target source over time. For field ID assignment see table 3.1. Colored by scan intent. Grey represents initial interferometer set up time and no data was collected during this time.

3.1.1 Observed Calibrators

The first calibrator observed was the quasar 3C138, or J0521+1638, which lies at a redshift of $z = 0.76$ (Geldzahler et al., 1984). This is a commonly used radio bright point-like polarized calibrator. 3C138 was used to calibrate antenna delay, flux density, bandpass correction, polarization position angle and cross-hand delay.

The complex gain calibrator, or phase calibrator, was J0157-1043. This radio source is a polarised quasar at $z = 0.616$ (SIMBAD Astronomical Database, n.d.). This was observed at regular intervals to be able to compensate for amplitude and phase fluctuations over time due to atmospheric and ionospheric fluctuations.

3C84 is a very radio bright unpolarized point source observed to calibrate for instrumental leakage between right and left hand polarization. J0359+5057 was also observed as an extra unpolarized source if anything would go wrong when observing 3C84.

The wideband Stokes I continuum intensity images of the calibrators as generated by the CASA pipeline can be seen in figure 3.3, with a center frequency of $\nu_c = 6.22$ GHz.

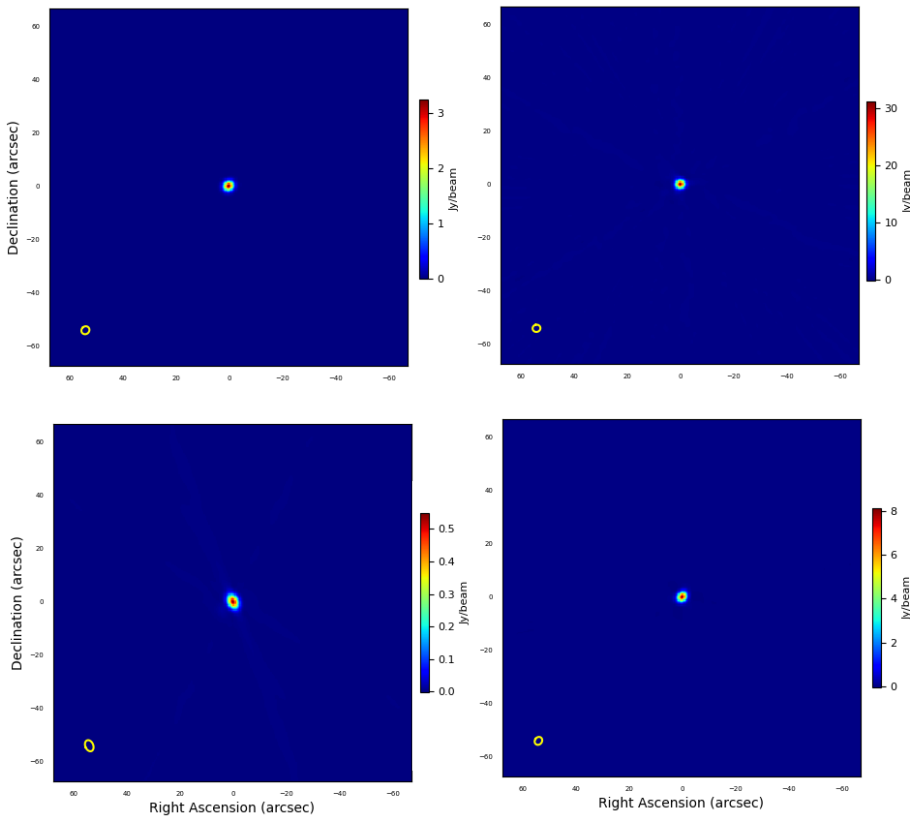

Figure 3.3: Top left: 3C138. Top right: 3C84. Bottom left: J0157-1043. Bottom right: J0359+5057. Imaged at a center frequency of $\nu_c = 6.22$ GHz. Synthesized beam in bottom left corner.

3.2 Data Calibration

After the raw data are collected by each antenna in the interferometer array they need to be correlated and calibrated. The dataset was first calibrated for hardware delays and Stokes I parallel-hand polarisation continuum by the automated VLA pipeline calibration process. After this calibration the dataset was manually calibrated for cross-hand polarisation, or Stokes Q, U and V.

The basic idea of data calibration for VLA is in principle simple. First a model of an observed calibrator is created for the physical property, e.g. intensity, that we wish to calibrate. Then a 'calibration table' is calculated such that when applied to the raw observed data of the calibrator the error between the calibrated data and the model data and is minimised. This calibration table is then applied to the observed target source.

3.2.1 Continuum (Stokes I)

For the Stokes I continuum calibration the VLA automatic calibration pipeline produced very good results. The pipeline starts by flagging non-usable data, such as

shadowed antennas, edge channels, periods of antenna slewing, radio interference etc. In the calibrated dataset, all data from the spectral window SPW28 (at a central frequency of $\nu_c \approx 5.7$ GHz) were completely flagged, along with antenna *ea*17 at a radial distance of ∼130 m from the center of the array. In total 34.6 percent of all collected data were flagged.

The dataset is then prepared for flux density strapping by importing an already known frequency dependent flux density model of the observed flux density calibrator 3C138 into the dataset. The flux density as a function of frequency for 3C138, taken from Perley and Butler (2017), can be seen in figure 3.4.

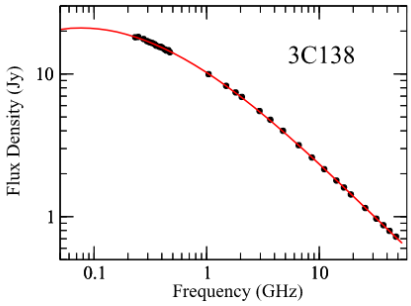

Figure 3.4: 3C138 flux density over frequency (Perley and Butler, 2017).

The pipeline then applies calibration tables to all observed data based on hardware and atmospheric conditions. This includes individual antenna delays, atmospheric opacity, antenna Gain-Elevation curves, etc. (Kimball, 2021). After this a band pass and delay calibration to correct for spectral response is made using 3C138. An initial gain calibration is also applied using the flux density model. In principle this applies a frequency-dependent gain to the observed flux calibrator data until it matches the model data, and the same gain table is applied to the observed target Double Irony.

The phase calibrator J0157-1043 is used for complex gain calibration, which corrects for amplitude and phase fluctuations that occur during the observation time by linearly interpolating phase and amplitude between phase calibration observations, as illustrated in figure 3.5. This calibrator is preferably one that has a low angular separation to the observed target. The complex phase gain tables are then applied to all data in the dataset.

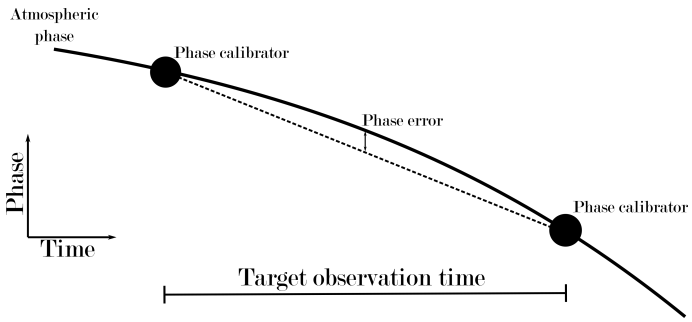

Figure 3.5: Phase calibrator observation over time

After all calibration tables have been applied to the data we can inspect the u, v amplitude distribution of our calibrators to get an rough idea of the quality of calibration. The u, v baseline length versus corrected amplitude distribution of 3C138 and J0157-1043 can be seen in fig. 3.6.

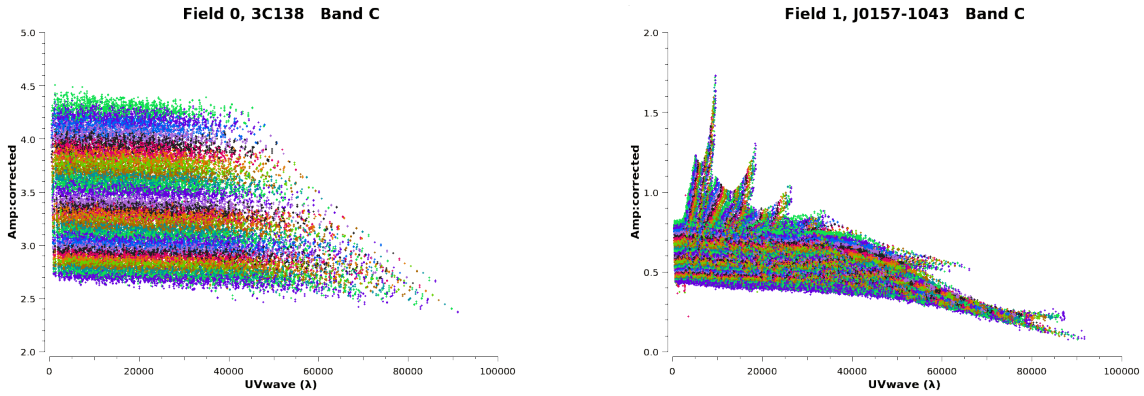

Figure 3.6: (u, v) baseline versus calibrated amplitude distributions for the flux density calibrator (left) and the phase calibrator (right). The colors represent different spectral windows.

The calibrated u, v baseline amplitude distribution of 3C138 looks like expected, where we see that the amplitude is highest for the first spectral window with the lowest center frequency (light green color band on top) and falls for higher spectral windows, and thus higher frequencies (each colored band represents one spectral window) as the spectral index of the source would predict. If the calibrator was a perfect point source we would expect each spectral window amplitude to be unchanged over different baselines, however the calibrator is slightly resolved, so we expect the amplitude to decrease with increasing baseline length. This is also observed in the calibrated data.

J0157-1043 however, shows some problems with the calibration tables. In the calibrated data we can see 'tendrils' of visibilities with a quickly increasing amplitude for shorter baselines. This calibrator is point-like at radio frequencies under 1.5 GHz for certain VLA configurations, however in C-band frequencies the quasar shows some

extended structure in all VLA configurations. The extended structure of J0157-1043 and its u, v amplitude distribution can be seen in figure 3.7, taken from the NRAO list of VLA calibrators (VLA Calibrators, n.d.).

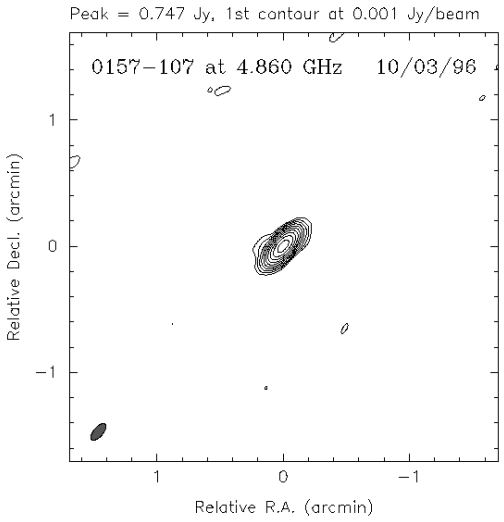

(a) J0157-1043 intensity contours

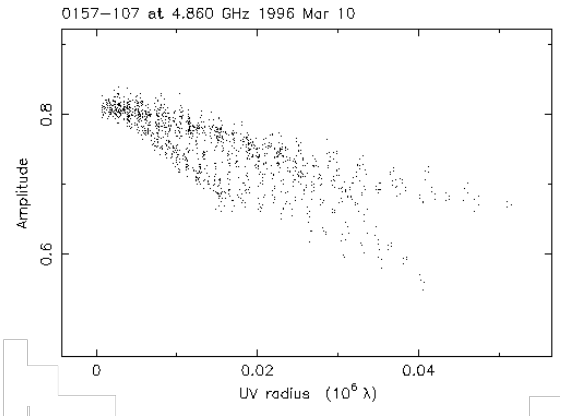

(b) J0157-1043 u, v amplitude distribution

Figure 3.7: J0157-1043 intensity and u, v amplitude distribution (VLA Calibrators, n.d.).

An attempt to remedy the calibration of J0157-1043 was made via an iterative self-calibration method using the NRAO computer cluster. However, self-calibration of the phase calibrator led to inferior noise level and dynamic range in the final images of the target compared to using the calibrations tables produced by the VLA pipeline.

3.2.2 Polarisation (Stokes Q,U,V)

While the VLA pipeline does not support polarisation calibration, the resulting continuum data from the pipeline were used as a starting point for polarisation calibration. Like the continuum calibration the first step is to build a model from known data. 3C138 was used again for polarisation angle and polarised intensity calibration. The polarisation properties in the C-band can be found in table 3.2, extracted from Perley and Butler (2013).

Frequency (GHz)	3C138 Frac. Pol. (%)	3C138 Abs. Pol. Angle (deg)
4.500	10.0	-11
5.000	10.4	-11
6.500	9.8	-12
7.250	10.0	-12
8.100	10.4	-10

Table 3.2: 3C138 polarisation angle and fractional polarisation from Perley and Butler (2013)

After this the polarisation-dependent antenna receiver delay is calibrated for. The R-L polarisation leakage, or instrumental polarization, also needs to be compensated for. The polarisation leakage is calibrated by observing a bright unpolarized source. In this case 3C84 was chosen. Next the R-L phase change over the frequency band needs to be calibrated, which affects the polarisation angle. Thus we need a calibrator with a known polarisation angle over frequency. Again 3C138 was chosen for this. Finally the calculated calibration tables are applied to the calibrators and the target source.

3.3 Imaging

After calibrating the data we can use the methods described in section 2.4 to produce clean images of our target source. The software used for this was CASA (Common Astronomy Software Applications) version 6.1.

3.3.1 Continuum Imaging

When imaging the whole frequency range of the C-band using the CASA function `tclean` we use the Multi-term Multi-Frequency Synthesis deconvolver, or 'MT-MFS', as this is well suited for large frequency bands. We use 'Briggs' weighting (see chapter 2.4.1) and set `'nterm=2'` to get two Taylor term images. It was found that setting the Briggs weighting 'robust' parameter to 0.0 gave a good dynamic range while still retaining relatively uniform noise. Lower robust parameters results in a smaller beam size and thus higher resolution, but higher noise levels. Higher robust values closer to a natural weighting gave a better dynamic range, but resulted in large areas with negative flux and artifacts in the noise. Fig 3.8 and table 3.3 show a comparison between two robust parameters scaled to increase noise visibility.

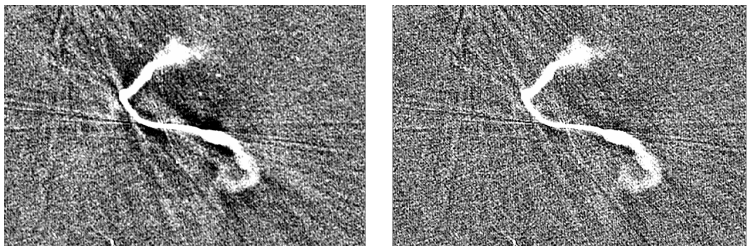

Figure 3.8: Comparison of Stokes I images using different robust parameters. Left: $R = 0.5$, Right: $R = 0.0$. Colors are scaled to increase noise visibility

Robust parameter	I_{max} (mJy/beam)	σ_I (µJy/beam)	Dynamic range (I_{max}/σ_I)	B_{Maj}	B_{Min}
0.0	1.243	3.20	383.2	$3.366''$	$2.653''$
0.5	1.298	2.78	467.0	$4.178''$	$3.267''$

Table 3.3: Comparison of image noise, angular resolution and dynamic range using different robust parameters.

The synthesized beam size and its frequency dependence can be seen in figure 3.9. As expected the angular resolution is better at higher frequencies.

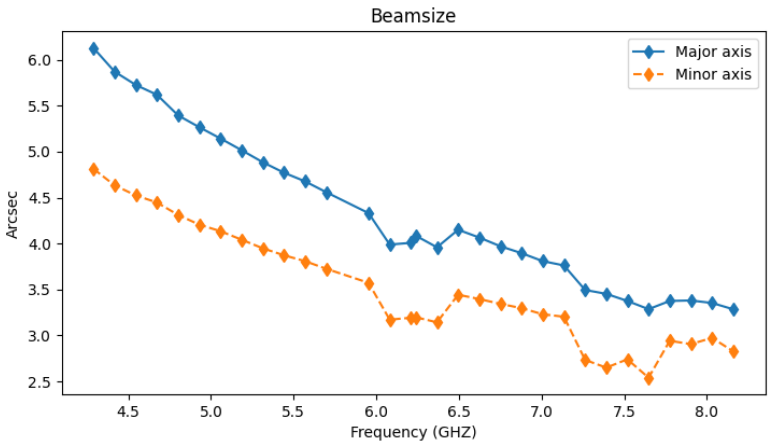

Figure 3.9: Major and minor axis in arcseconds of the synthesized beam over frequency.

3.3.2 Fractional Polarisation

The fractional polarisation p is defined as the ratio of polarised flux density to total flux density. We first define the linearly polarised flux density as

$$I_p = \sqrt{Q^2 + U^2} \tag{3.1}$$

However this I_p flux density will have a bias due to the fact that Gaussian noise in the Stokes Q and U data is distributed around 0. When we square the intensity data the resulting positivity of the noise creates an asymmetric Rayleigh distribution of noise (Sohn, 2011). This in turn creates a bias in I_p. A good approximation of the solution to this problem as described by Wardle and Kronberg (1974) is

$$I_{p,obs} = \sqrt{I_p^2 - \sigma_p^2} \tag{3.2}$$

where σ_p is the RMS of the noise distribution in the polarised intensity map.

After obtaining the corrected linearly polarised intensity we can make a map of the fraction of linear polarisation p by dividing $I_{p,obs}$ by the Stokes I flux density I as

$$p = \sqrt{\frac{I_{p,obs}^2}{I^2}}. \tag{3.3}$$

Since we are dividing with the Stokes I intensity, we risk dividing with values approaching zero when working in areas close to the noise level of the Stokes I emission. Thus when making our fractional polarisation map we only considered areas where the Stokes I intensity is over $5\sigma_I$.

3.3.3 Linear Polarisation Angle

We use the equation 2.23 to calculate the polarisation angle given Stokes Q and Stokes U data. Unlike the fractional polarisation there is no need to compensate for a Rician bias in the polarisation angle. Since we are not taking the absolute value of any intensity, the noise distribution remains symmetric (Sohn, 2011).

To make sure we are not including the polarisation angle of thermal noise, we want to limit our polarisation angle map to areas where the sum of Stokes Q and Stokes U is above thermal noise levels. Thus we limit our polarisation angle map to some limit of polarisation noise $I_{p,obs} > 2\sigma_{p,obs}$.

When imaging we also give equation 2.23 an offset of $\pi/2$ rad to give a visual representation of the magnetic field lines, as they are orthogonal to the linear polarisation angle of the electric field lines.

3.3.4 Rotation Measure Synthesis

To correct polarimetric data for the effect of Faraday rotation, a software called *pyrmsynth*[1] by Michael Bell was used. This software uses direct Fourier transform to produce dirty images corrected for Rotation Measure along the line of sight to the source. It also supports a 'RM CLEAN' method, described in Heald (2009), to deconvolve the complex polarisation from the rotation measure spread function (RMSF). The RMSF is analogous to the point spread function, or dirty beam, but in the Faraday depth space.

[1] https://github.com/mrbell/pyrmsynth

The RMSF, or resolution in Faraday depth space $\delta\Phi$, is determined by the frequency range of the measurement data by $\delta\Phi = 2\sqrt{3}/\Delta\lambda^2$ where $\Delta\lambda^2 = \lambda^2_{max} - \lambda^2_{min}$. λ_{min} and λ_{max} are the minimum and maximum wavelengths in the observed frequency band. The largest resolved scale in Faraday space is given by π/λ^2_{min}. The maximum observable Faraday depth, Φ_{max}, is determined by the wavelength range $\delta\lambda^2$ of the individual spectral windows used in the rotation measure synthesis via $\Phi_{max} = \sqrt{3}/\delta\lambda^2$. The calculated values for these quantities can be seen in table 3.4.

Parameter	Value	Description
Φ_{max}	5936.8 rad/m^2	Maximum observable Faraday depth
$\Phi_{max\ scale}$	2362.4 rad/m^2	Maximum resolved scale in Faraday depth
λ^2_{min}	1.33 $\times 10^{-3}$ m^2	Minimum wavelength
squared λ^2_{max}	5.03$\times 10^{-3}$ m^2	Minimum wavelength squared
$\delta\Phi$	934 rad/m^2	RMSF
$\delta\nu$	128 MHz	Spectral window width (frequency)
$\delta\lambda^2$	0.292$\times 10^{-3}$ m^2	Spectral window width at 4.22 GHz
$\Delta\lambda^2$	3.71 $\times 10^{-3}$ m^2	Complete bandwidth λ^2_{max} - λ^2_{min}

Table 3.4: Faraday space parameters from the observed data

4

Results and Discussion

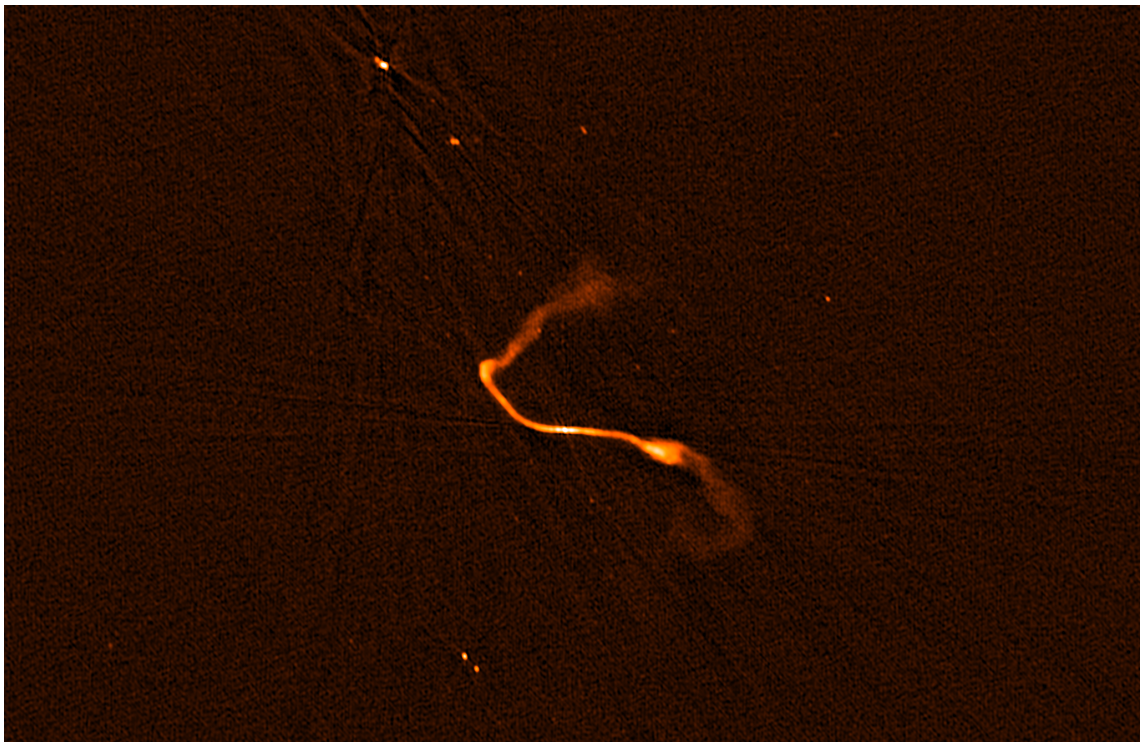

Figure 4.1: Deconvolved and cleaned image depicting wideband Stokes I continuum (4.2-8.2 GHz) of Double Irony. The angular size of image is approximately 16.6×10.8 arcminutes, with a synthesised beam of $3.37'' \times 2.65''$

4.1 Stokes I Continuum Intensity

The wideband Stokes I continuum was generated using the CASA 6.1 method `tclean` using the parameters specified in table 4.1. Spectral window 28 was excluded in the wideband imaging due to noise. The images have a background RMS noise of $\sigma \approx 3.2$ µJy/beam and a maximum brightness I_{max} of 1.24 mJy/beam, resulting in a dynamic range of $I_{max}/\sigma \approx 383$. The histogram of the noise distribution of an empty area next to Double Irony can be seen in figure 3.8.

$N_{iterations}$	20 000
Residual Threshold	15 µJy/beam
Resolution	2048x2048
Cell size	0.5″
Weighting	Briggs
Robustness	0.0
Deconvolver	MT-MFS
Taylor terms	2
Scale Sizes	0, 6, 24 px

Table 4.1: `tclean` parameters for Stokes I continuum images

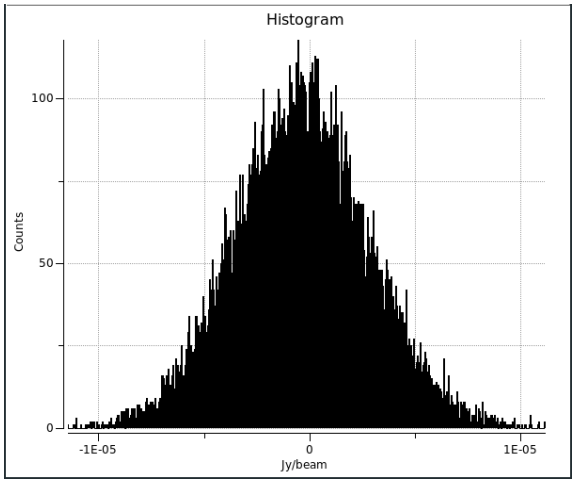

Figure 4.2: Distribution of background noise in the cleaned Stokes I continuum image, measured in an empty area.

The wideband image in fig. 4.1 has a resolution of 0.5″ per pixel, with a scale of 2.443 kpc/″ at the relevant redshift. In fig 4.3 the Double Irony object is visualised using an inverse hyperbolic sine color scale. The synthesised beam size is 3.37″ × 2.65″.

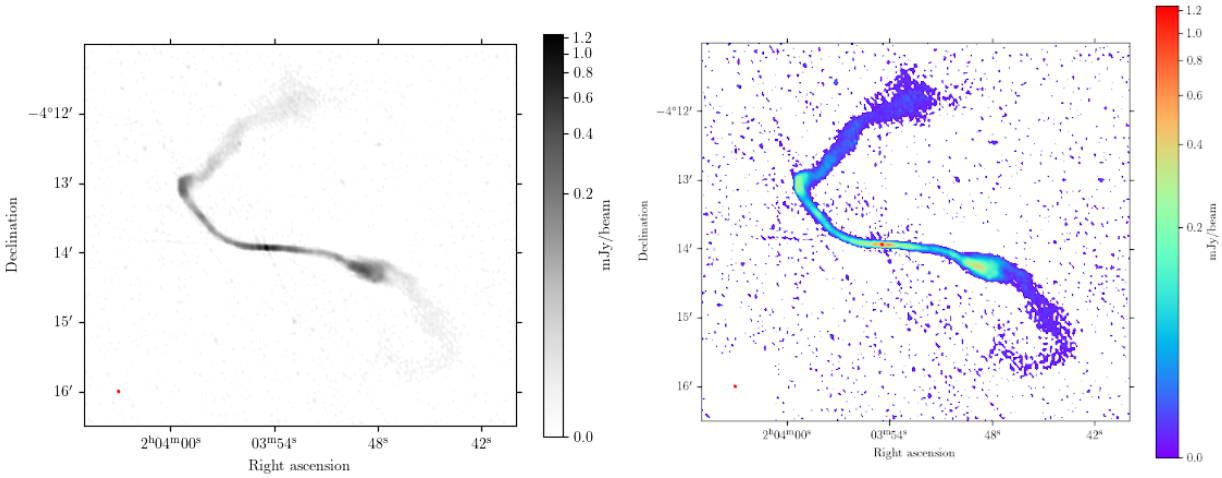

Figure 4.3: Wideband frequency Stokes I continuum (4.2-8.2 GHz) of Double Irony, visualised using two different color scales. Noise below 2σ masked out. Synthesised beam visualised in red in bottom left corner. Bottom left corner emissions are excluded for visual clarity of synthesised beam.

In figure 4.4 we can see a close-up on the central area around the galaxy in the center of the Double Irony structure. We can see blobs of emission on both sides of the core.

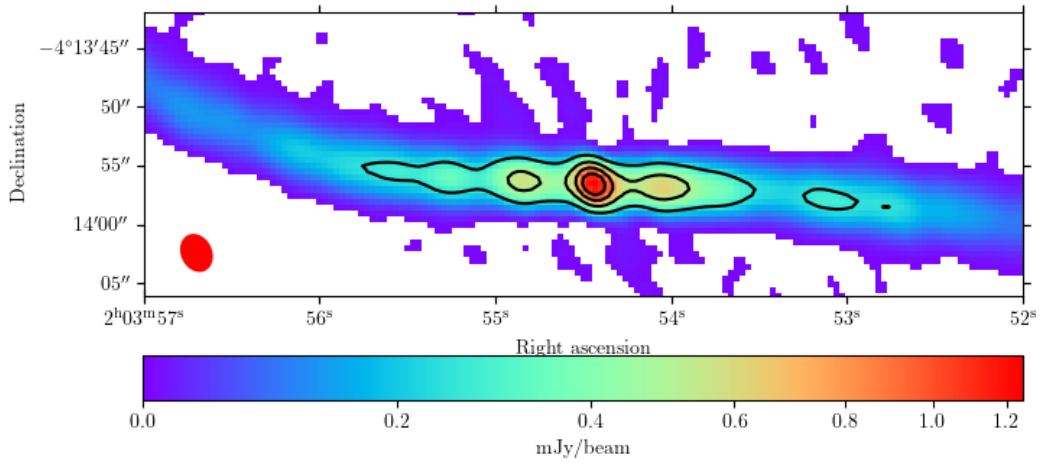

Figure 4.4: Closeup on the area around the central core. Contours at 0.25, 0.50, 0.75 and 1 mJy/beam

4.1.1 Spectral Index

To calculate the spectral index, two different methods were used. The first method uses CASA `tclean` to calculate the spectral index map via a MT-MFS deconvolution algorithm. The other method considers the intensities of each separate spectral

window, and does a fit to the intensity data over frequency for each pixel to determine the spectral index.

The interferometer sensitivity falls of with increasing distance from the center due to primary beam attenuation. This effect is dependent on frequency. In the first method, a CASA function *widebandpbcor* for correcting beam attenuation of MT-MTS wideband images was used. In the second method, all spectral windows were individually corrected for primary beam attenuation during `tclean`.

Using the MT-MFS deconvolution with at least 2 Taylor terms CASA generates the spectral index map and spectral index 1σ error map. This data are masked at $I < 3\sigma_{RMS}$, where the RMS noise is measured close to the SW2 plume, as the primary beam correction increases the noise levels in this area. The resulting spectral index map and the corresponding uncertainty map can be seen in figure 4.5.

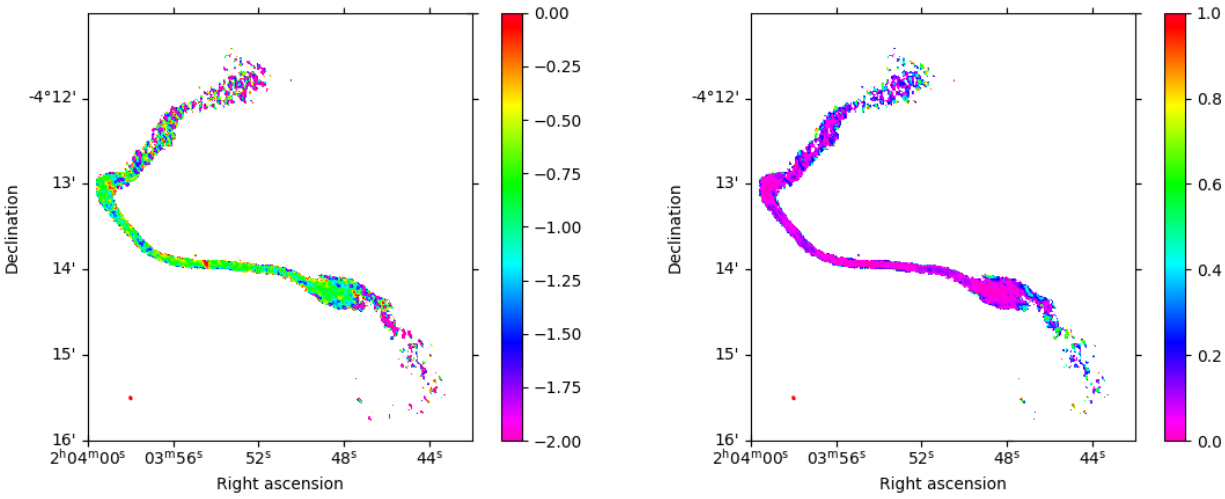

(a) Spectral index α map

(b) Spectral index error σ map

Figure 4.5: Spectral index map with 1σ uncertainty, obtained with the MT-MFS deconvolution method.

The southwest plume and northern plume intensity levels are very close to the RMS noise in higher spectral windows (see Appendix A.1) and the spectral index appears to have local, large fluctuations with a high uncertainty in these areas. Pictured in figure 4.6 is the area consisting of the central core and the two jets.

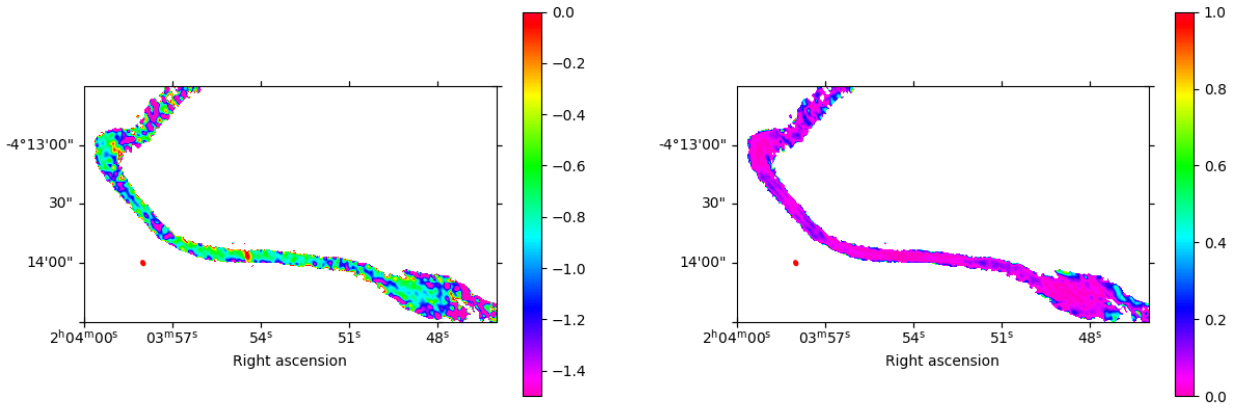

(a) Spectral index α map.

(b) Spectral index error σ map

Figure 4.6: Left: Spectral index map of the central part of the Double Irony. Note the change in color scale. Right: 1σ uncertainty map

Here the central core shows a spectral index around 0, with a slightly positive maximum value of $\alpha = 0.022 \pm 0.014$. This is expected due activity in the core, accelerating electrons. The spectral index then tapers of towards steeper negative values in the jets, signifying synchrotron radiation with an aging electron population as the distance from the core increases. The spectral index significantly tapers of towards the plumes. In the Elbow and SW1 area the spectral index rises slightly, which might indicate an injection of high energy electrons, possibly due to shock waves.

An alternative method for determining the spectral index was used for comparison with the CASA method. All spectral windows of bandwidth 128 MHz were individually deconvolved and cleaned with a restoring beam of constant size. The beam was constructed using the spectral window with the lowest frequency, and thus the largest beam. Table 4.2 specifies the `tclean` parameters used. SPW 28 was excluded due to noise.

$N_{iterations}$	20 000
Residual Threshold	40 µJy/beam
Resolution	2048x2048
Cell size	$0.5''$
Weighting	Briggs
Robustness	0.5
Deconvolver	Högbom
Taylor terms	1
Beam_{MAJ}	$6.3''$
Beam_{MIN}	$4.86''$
Beam_{PA}	$27.2°$

Table 4.2: `tclean` parameters for spectral windows used in spectral index calculations and Rotation Measure synthesis.

By "stacking" the spectral windows, every pixel position has a frequency domain, where the Stokes I flux density is a function of frequency via $I(\nu) = \nu^{\alpha}$. Using the logarithm of the Stokes I intensity $\log(I_\nu)$ and frequency $\log(\nu)$, a least-square fit over the frequency domain at every pixel of the image is done via

$$E = \sum_{j=0}^{k} \Big| \log(\nu_j) p(0) + p(1) - \log(I_j) \Big|^2 \tag{4.1}$$

where $p(0)$ and $p(1)$ are the parameters of the fit. This is done using the python function *numpy.polyfit*. From this we get α and 1σ standard uncertainty on the fit. This method is visualised in fig. 4.7 for three positions in Double Irony, marked in fig. 4.8. Data under $3\sigma_{RMS}$ is not included in the fit.

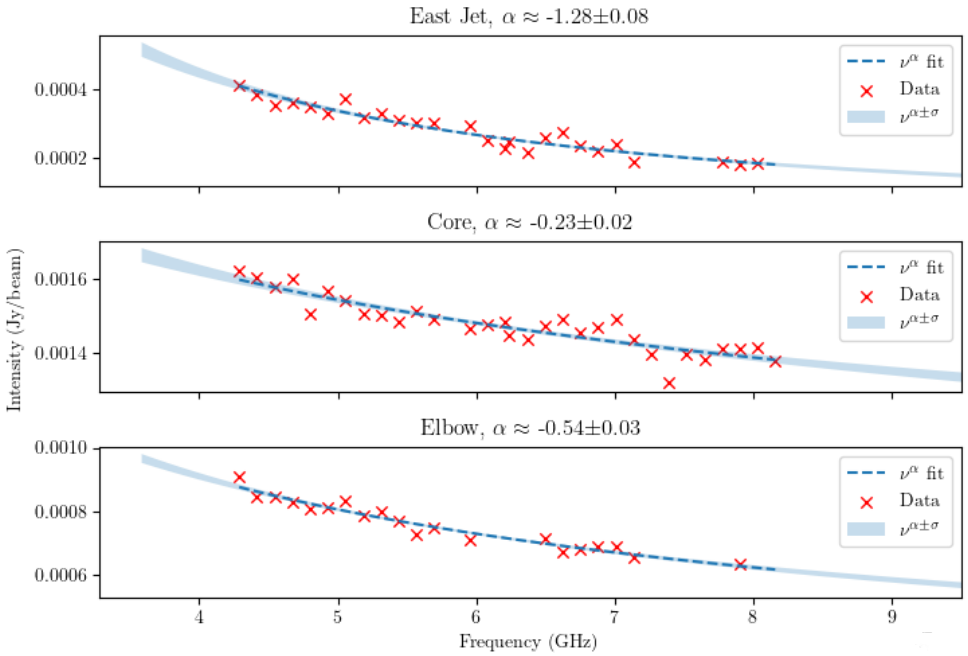

Figure 4.7: Least square fit of $I(\nu) = \nu^\alpha$ with 1σ error at three different positions in Double Irony

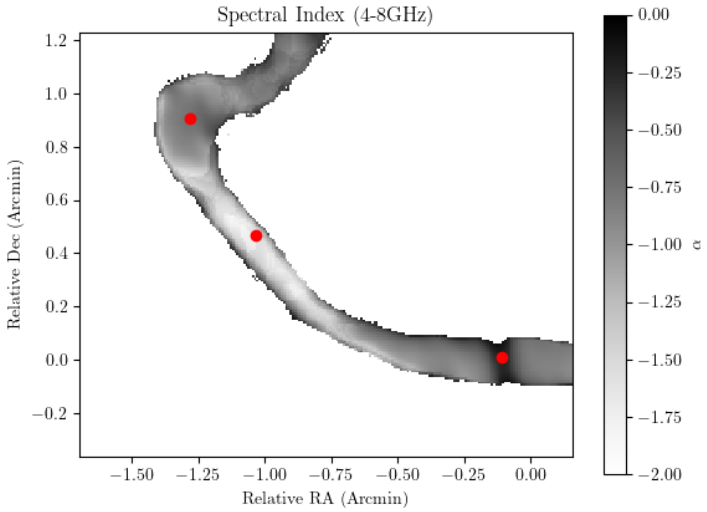

Figure 4.8: Marked in red: Positions of spectral index fit used for figure 4.7

Only pixels with more than 30% of frequency data unfiltered are considered. This prevents an over/under estimation of α due to data exclusion. The resulting spectral index map and its uncertainty can be seen in figure 4.9

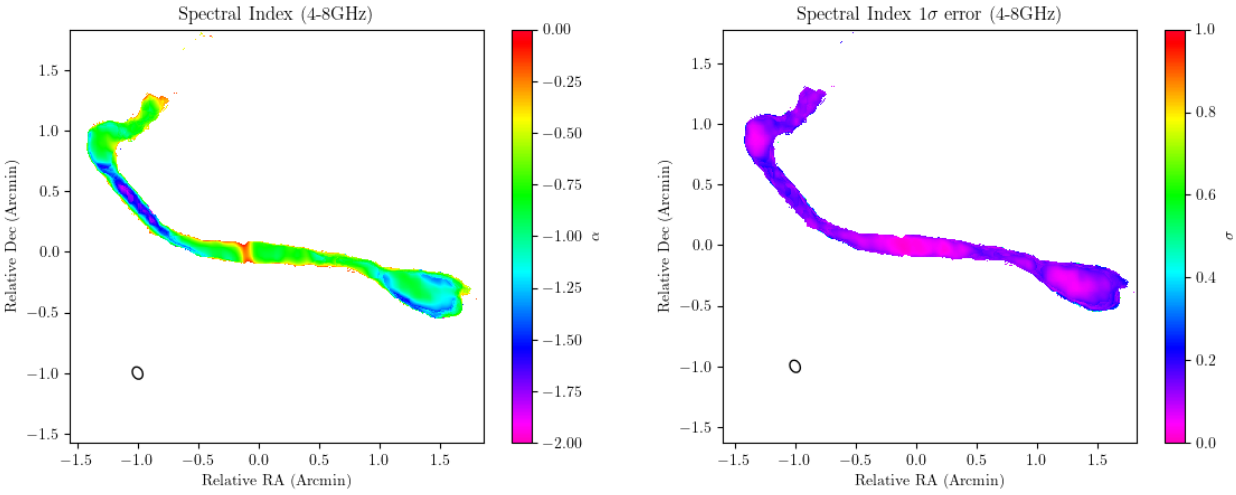

(a) Spectral index α map **(b)** Spectral index error σ map

Figure 4.9: Spectral index map with 1σ uncertainty obtained by fitting a power law to the intensities in the individual spectral windows. Synthesised beam marked marked by ellipse in bottom left corner.

Using this method sacrifices some angular resolution since all individual spectral windows are restored using the same beamsize, set by the lowest frequency observed. Nonetheless it appears to be a viable method, and produces results in decent agreement with the CASA method.

In figure 4.10 we can see a spectral index map from earlier data, with spectral index (left) and error map (right) from a lower frequency band at 2-4 GHz for comparison (Montoya Arroyave, 2019).

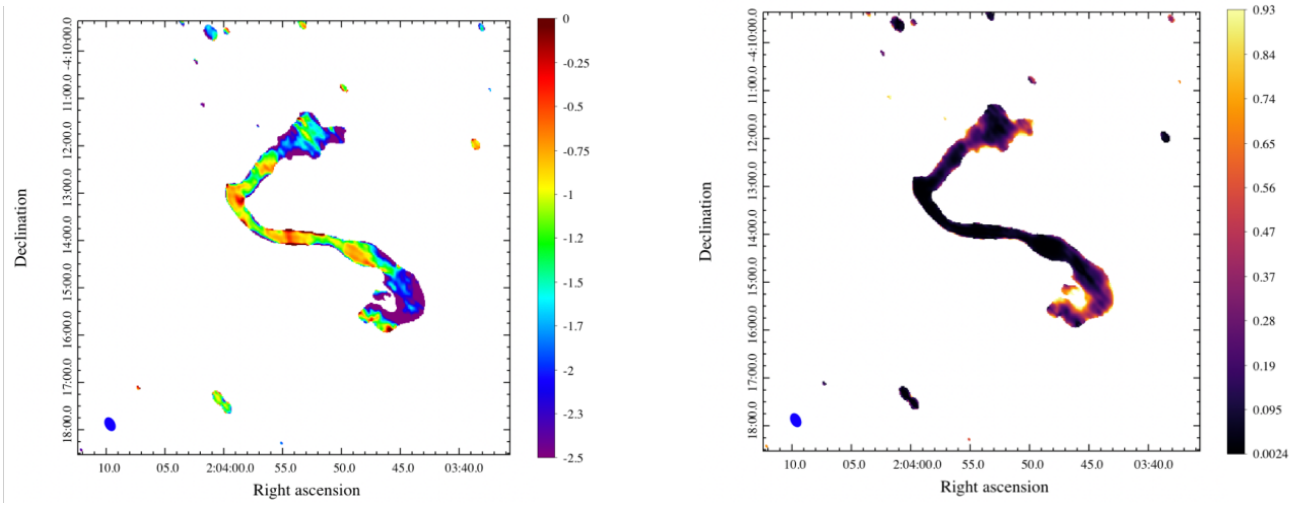

(a) Spectral index α map

(b) Spectral index 1σ error map

Figure 4.10: Earlier data of Spectral index map (left) with error map (right) from a lower frequency band at 2-4GHz (Montoya Arroyave, 2019). Synthesised beam marked in blue in bottom left corner.

There is also a good correlation between old data in fig 4.10 with the new data, with a spectral index approaching zero in the core, and steeper values in the outer plumes. However one curiosity seen in the 2-4 GHz dataset and hinted at in the 4-8 GHz dataset is the area of shallow spectral index in the northeastern plume, where the spectral index again approaches zero in both datasets. In the east jet there is an area before the Elbow where the spectral index drops sharply. In the manually fitted data this effect is much more pronounced than in the data generated by CASA, however the CASA data still shows the same trend.

4.2 Polarimetry

Since the polarisation data might have a frequency dependent depolarisation affecting wideband data, this chapter will first examine the polarisation data for spectral window 16 with a center frequency of 4.29 GHz and a 128 MHz band, together with uncorrected wideband data. The concluding section of this chapter will treat wideband data using Rotation Measure synthesis and spectral cleaning.

4.2.1 Stokes Q,U,V

In figure 4.11 we can see the three Stokes parameters Q,U and V for spectral window 16 with a center frequency of 4.29 GHz and a 128 MHz bandwidth.

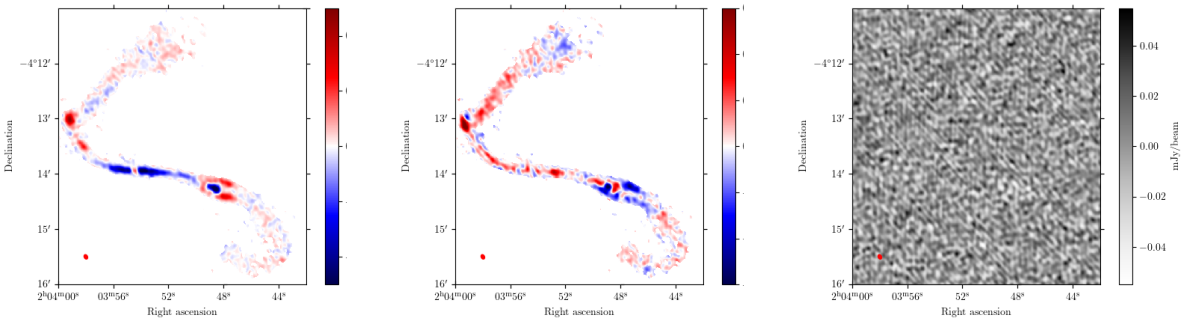

(a) Stokes Q **(b)** Stokes U **(c)** Stokes V

Figure 4.11: Stokes parameters imaged. Centered at 4.29 GHz with a 128 MHz band. Beam visualised in bottom left corner. Stokes V parameter not masked.

We do not expect to see any circularly polarised intensity, and in figure 4.11c there is as expected no brightness over thermal noise in our Stokes V data. This indicates that we have good calibration of polarisation in this spectral window.

4.2.2 Fractional Polarization and Polarisation Intensity

Using data from figure 4.11 the polarisation intensity is calculated according to the method in 3.3.2. In figure 4.12 the resulting polarised intensity for the spectral window at 4.29 GHz can be seen, as well as a wideband image of polarised intensity before RM correction. The Ricean bias is compensated for with a $\sigma_{RMS,p} \approx 13$ µJy/beam in SPW 16 and $\sigma_{RMS,p} \approx 2.7$ µJy/beam in the wideband image.

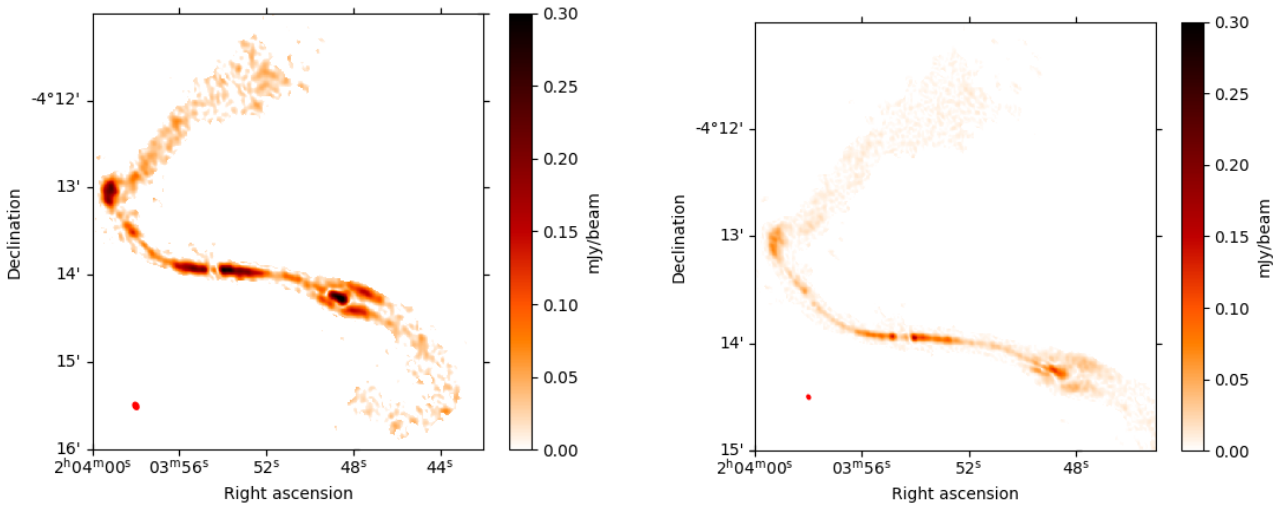

Figure 4.12: Left: Linear polarisation intensity of SPW 16 (centered at 4.29 GHz with a 128 MHz band). Synthesised beam in red in bottom left corner ($6.3'' \times 4.86''$). Right: Wideband linear polarisation intensity not corrected for Faraday rotation. Synthesised beam is $3.37'' \times 2.65''$. Note that the angular size of the images are different.

The fractional polarisation filtered at $5\sigma_I$ can be seen in figure 4.13. Polarised intensity contours at levels 0.067, 0.13 and 0.20 mJy/beam are overlaid.

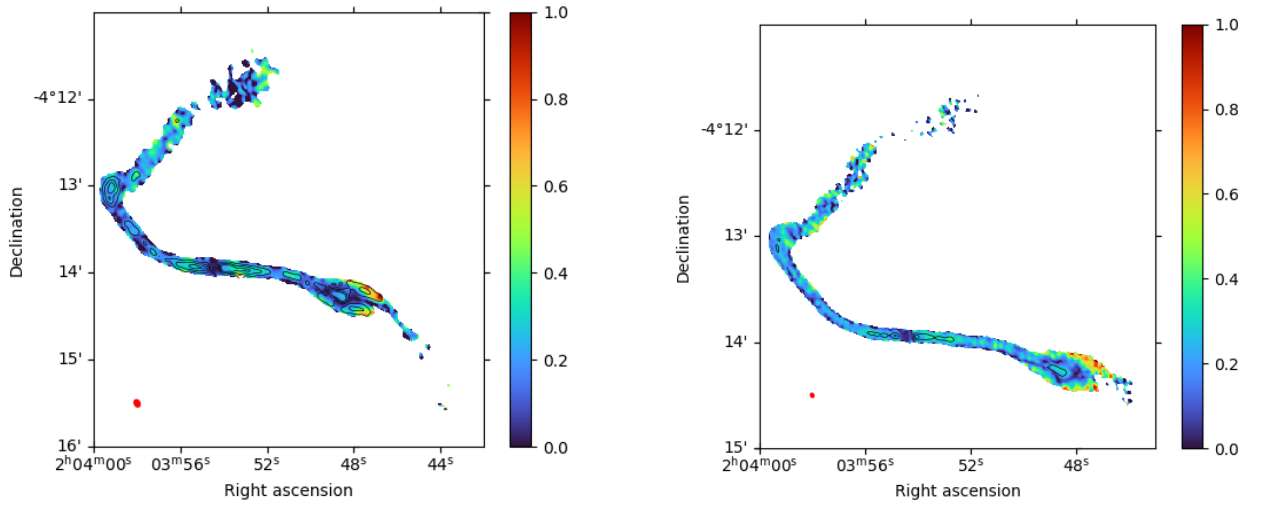

Figure 4.13: Left: Fractional polarisation intensity centered at 4.29 GHz with a 128 MHz band. Linear polarisation intensity contours overlaid at 0.067, 0.13 and 0.20 mJy/beam. Right: Wideband polarisation fraction, uncorrected for rotation measure.

Based on the spectral index map and the relation between spectral index and polarisation degree via equation 2.24, the theoretical degree of polarisation is around 60-75% throughout the Double Irony galaxy. This indicates that depolarisation occurs, possibly though disordered magnetic fields in the source or Faraday dispersion in front of the source.

4.2.3 Rotation Measure

The *pyrmsynth* method was applied on a stack consisting of Stokes Q and Stokes U data for each spectral window. Each spectral window was restored with a constant beam size using the parameters specified in table 4.2. The rotation measure synthesis and corresponding RM-CLEAN was performed using the parameters specified in table 4.3, where the cutoff value is based on similar rotation measure synthesis work in Kierdorf et al. (2020).

Parameter	Value	Description
Φ_{min}	-2500 rad/m^2	Minimum Faraday depth
N_Φ	1000	Number of steps
$d\Phi$	5 rad/m^2	Step size
N_{iter}	1000	RMCLEAN max iterations
γ	0.1	RMCLEAN loop gain
cutoff	$6\sigma_{QU}$ (78 mJy/beam)	RMCLEAN residual threshold
Φ_{FWHM}	415 rad/m^2	Fitted FWHM of RMSF

Table 4.3: Parameters used for RM synthesis and RM CLEAN

The resulting RMSF can be seen in figure 4.14.

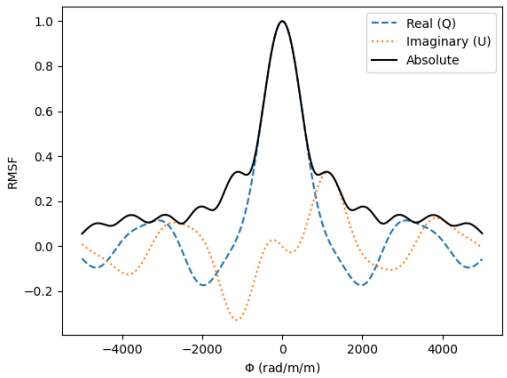

Figure 4.14: Rotation measure spread function

CLEANed Stokes Q, Stokes U and ϕ Faraday depth cubes were obtained. The 2-dimensional Stokes Q and Polarised intensity maps visualised in figure 4.16 are

determined by sampling the maximum values of polarised intensity along the line of sight to the source for each pixel.

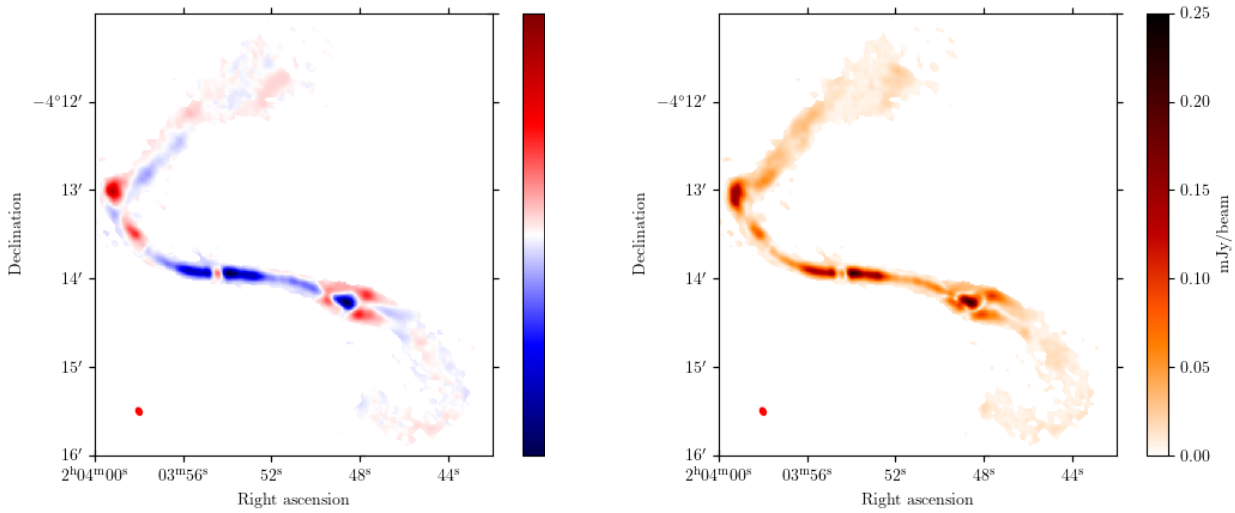

Figure 4.15: Wideband image after correction via Rotation Measure synthesis. Stokes Q (left) and polarisation intensity (right)

The Faraday depth ϕ can be seen in figure 4.16, masked at $I_{p,RM} < 2\sigma_{p,RM}$ where $\sigma_{p,RM}$ is the wideband averaged RMS noise of the corrected polarised intensity map.

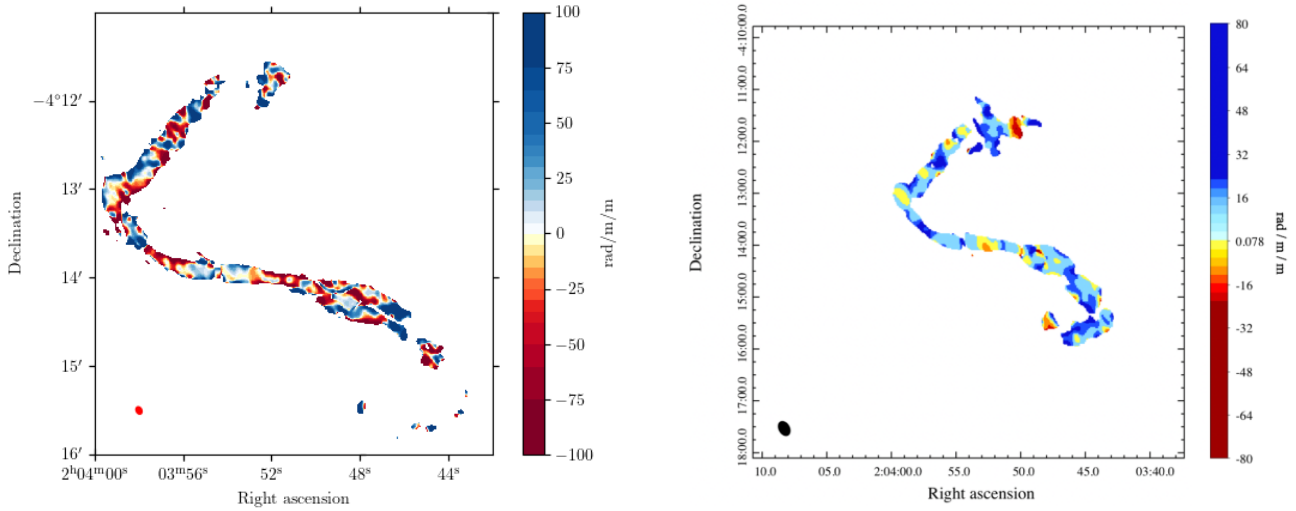

Figure 4.16: Rotation measure of 4-8 GHz (left) and 2-4 GHz (right). 2-4 GHz data from Montoya Arroyave (2019). Note the difference in angular size of the images, and the difference in synthesised beam size.

Positive values of ϕ are indicative of a magnetic field component pointing towards the observer along the line of sight from the source, while negative ϕ values indicate magnetic field lines pointing towards the source along the line of sight. Considering the C-band data at 4-8 GHz we can observe low positive values around the core structure, while both jets change to positive values of ϕ further away from the core. In the elbow and along the northern plume there is a pattern of positive RM along one edge of the elbow and plume, with negative values on the other edge, running in parallel, transverse to the jet direction. Such a gradient could indicate a toroidal magnetic field component (Wardle, 2013). Another area of interest is the center of SW1. In the same spot we observe the peak polarised intensity in SW1, the Faraday depth falls to < 5 rad/m^2. There seems to be a general correlation between high polarised intensity and low Faraday depth, as expected from the Faraday depolarization effect of Faraday rotation.

There is a discrepancy between 2-4 GHz data and 4-8 GHz data in many areas. This could be due to a change in depolarization dependent of frequency, or a effect of the higher angular resolution and lower Faraday depth resolution of the higher frequency data. The distribution of Faraday depth over Double Irony can be seen in fig. 4.17.

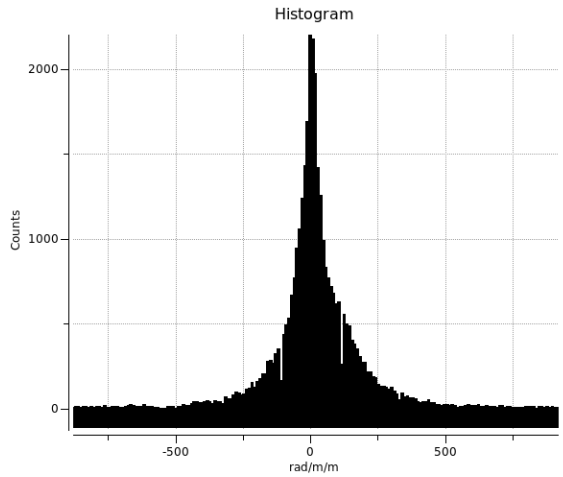

Figure 4.17: Histogram of RM (Faraday depth) values, ϕ.

4.2.4 Linear Polarisation Angle

The linear polarisation angle data is calculated using Stokes Q and Stokes U data, as such the linear polarisation angle might also be affected by Faraday rotation. First the polarisation angle data for a single spectral window with a center frequency of 4.29 GHz and a 128 MHz band, not corrected for rotation measure, is calculated. After this the wideband polarisation data correcting for rotation measure synthesis and spectral cleaning will be examined.

Polarisation angle data is calculated using equation 2.23 using Stokes Q and Stokes U data, and is masked at $I_{p,obs} < 2\sigma_{QU}$, where σ_{QU} is the 4.29 GHz Stokes Q and

U average RMS noise of around 13 µJy/beam. The polarisation angle data has an added offset of $\pi/2$ rad to visually represent the magnetic field lines in the plane of the sky.

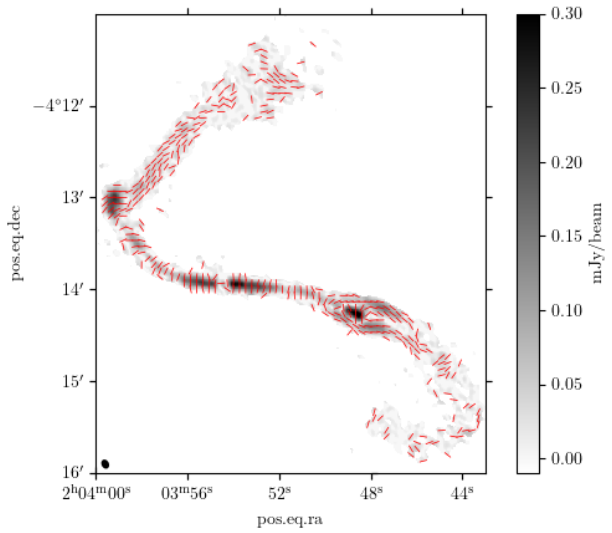

Figure 4.18: SPW 16 linear polarisation angle overlaid on polarisation intensity.

Using the RM corrected polarisation data, the wideband linear polarisation data is then calculated, fig. 4.19.

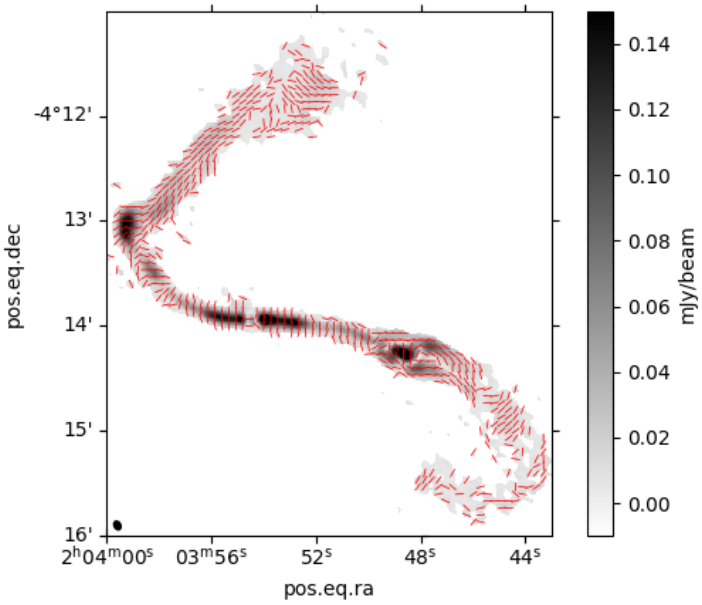

Figure 4.19: RM corrected wideband polarisation angle (red) overlaid on RM corrected wideband polarization intensity in grey

A closeup of the different areas can be seen in fig 4.20 and fig. 4.21.

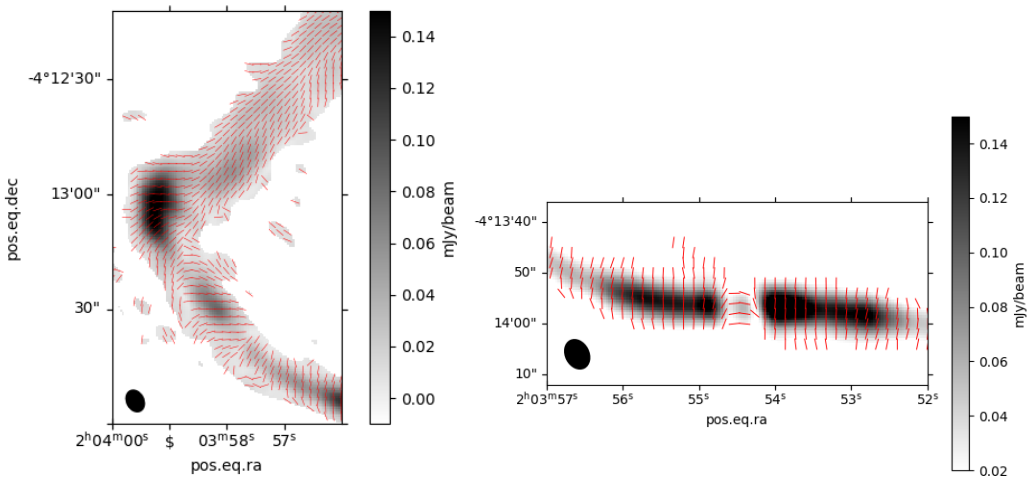

Figure 4.20: Closeup of polarisation angle of the Elbow (left) and core (right), overlaid on polarisation intensity.

In the jet extending out from the core the magnetic field is aligned transverse to the jet, which could indicate compression of a disordered magnetic field by a shock. It could also be a helical field in the expanding jet from the core, with a pitch angle greater than 45 deg (Wardle, 2013). In the elbow there as a change in magnetic field direction, and the magnetic field is aligned parallel to the north plume until the end of the plume, where it aligns transverse to the plume.

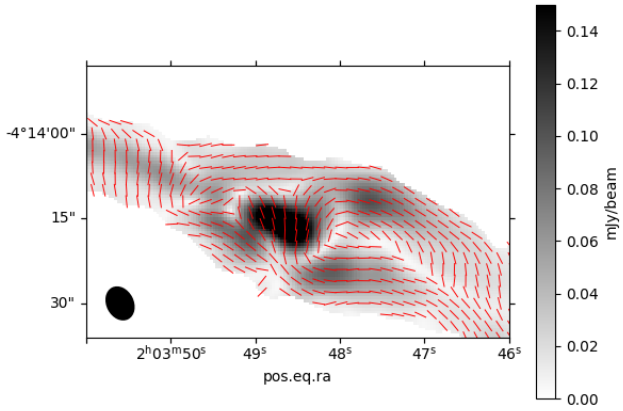

Figure 4.21: Closeup of polarisation angle of the SW1 area, overlaid on polarisation intensity.

In the SW1 structure, there are magnetic field lines moving in parallel along the

jet direction, with an area of transverse field lines in the highly polarised center structure.

The resulting data has a much higher angular resolution than the polarisation angle analysed in SPW 16, while simultaneously having a lower noise level in Stokes Q and Stokes U. Thus the magnetic field lines in the plumes are more visible. In the outer edges of the north plume there seems to be a component of magnetic field aligned at a 45deg angle from the field lines parallel to the plume. There is also an abrupt transition between longitudinal and transverse field lines towards the end of the north plume. A similar change from longitudinal and transverse field lines happens in the SW2 plume. In the SW1 structure we can also note that the magnetic field lines aligned parallel with jet around the polarised area does not join together completely smoothly towards the plume.

The effect of rotation measure correction on the wideband linear polarisation data are visualised in figure 4.22. The polarisation angle data are masked at $I_p < 2\sigma_p$, where σ_p is the uncorrected wideband averaged polarisation intensity RMS noise. This masking is more aggressive, as the uncorrected data is less smooth and does not produce as good polarisation angle data in the north plume and some areas of the east jet. This is in part due to different deconvolution algorithms used for the uncorrected wideband data and the corrected wideband data.

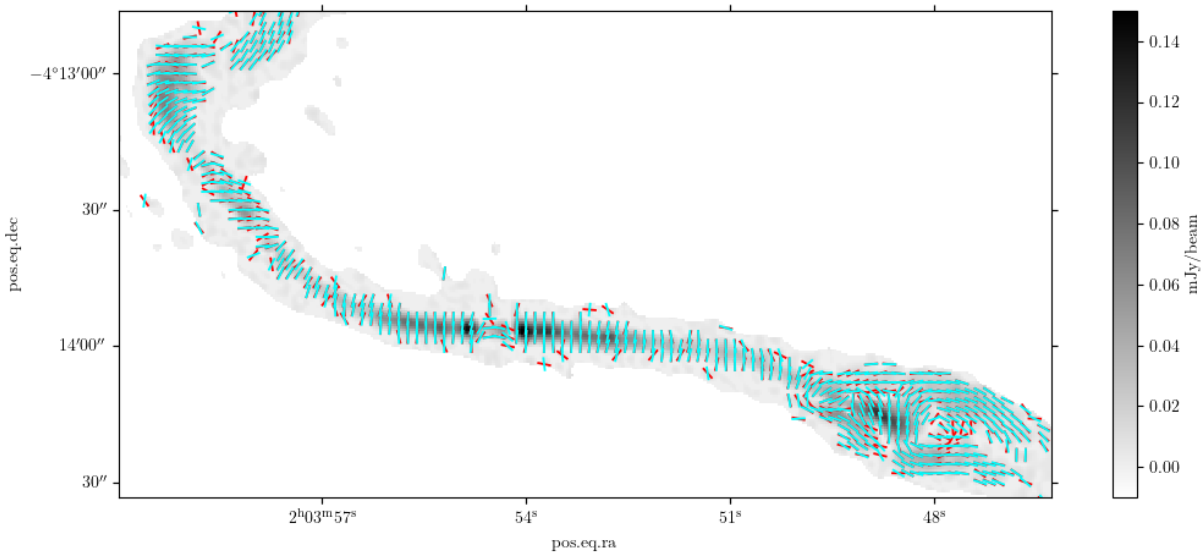

Figure 4.22: Wideband rotation measure polarisation angle (cyan) overlaid on wideband polarisation angle (red). Polarisation intensity in grey

The corrected field lines cover most of the uncorrected field lines, implying there is little or no change in polarisation angle. The isolated field lines with a large angular separation along the edges is likely due to noise. However looking close along the southeastern edge of the elbow, the center of the eastern jet, and the area

of SW1, there is a slight but noticeable angular separation between the corrected and uncorrected data.

5

Conclusion

Using the VLA pipeline, the Stokes I continuum was successfully calibrated. The phase calibrator did have a slightly resolved structure in the C-band which might have had an effect on calibration. After imaging the Stokes I continuum the wide-band image has a good dynamic range and a high angular resolution compared to earlier data. However some artifacts are left in the image, which can be seen around the core and around nearby bright sources. These artifacts could be from calibration errors or from nearby bright sources. The resulting Stokes I images clearly shows the iconic structure of Double Irony, with the twisting jets and plumes visible. Towards the higher end of the frequency range the plumes are difficult to resolve from the surrounding noise.

Spectral index maps were imaged using both a CASA method for spectral index calculations via primary beam corrected wideband MT-MFS deconvolved images and by manually calculating the spectral index from primary beam corrected invididual frequency bands. The CASA method agrees well with earlier literature and provides a high resolution spectral index map. The optically thick core and optically thin jets have spectral values within expected ranges, indicating synchrotron emission with older electron populations with increasing distance from the core. The manually computed spectral index map shows decent agreement with the CASA data, and the method seems viable if multiple Taylor term wideband imaging is not available.

Manual polarisation calibration using the VLA pipeline output as a starting point produced good results. The resulting polarised intensity images shows correlation with earlier work, but with a higher angular resolution. The individual spectral windows shows no structure in Stokes V, hinting at good data and calibration. By correcting for rotation measure using RMCLEAN the RM corrected wideband polarisation intensity and Stokes Q and Stokes U data were computed. The Faraday depth distribution appears to be in agreement with earlier data, however the Faraday depth map differs in most regions. The Rotation Measure spread function is quite wide in Faraday depth space due to the high frequency band of the data. The Rotation Measure gradients along the Elbow and north plume might indicate a toroidal magnetic field component. Earlier work suggests a toroidal field component along the west jet as well, with a Faraday depth gradient transverse to the jet direction. This feature is also observed in both jet directions in this work.

Wideband RM corrected polarisation angle data shows many features around the different regions of Double Irony. The magnetic field line vectors are well ordered and clearly visible in the polarimetry data. The core shows magnetic field lines perpendicular to the jets, with the magnetic field in the jets transverse to the jet direction. This might indicate a helical field with a pitch angle greater than 45 degrees, or a shock compressing a previously disorderly magnetic field. The magnetic field shows a very peculiar structure around the SW1 area, with areas of magnetic field lines seemingly twisting around a highly polarized central area.

5.1 Future Work

Combining the spectral range of the measurement set used in this work with earlier similar work at longer wavelengths would result in a good Faraday depth resolution together with high spatial resolution. The magnetic field in the SW1 area is worthy of further analysis.

Creating simulation models of the jets and the magnetic fields to correlate with the observed data could provide more information on the behaviour and structure of the jets in Double Irony. Further analysis of the jets and plumes could shed more light on their interaction with the surrounding medium.

Bibliography

M. A. Brentjens and A. G. de Bruyn. Faraday rotation measure synthesis. *Astronomy & Astrophysics*, 441(3):1217–1228, October 2005. doi: 10.1051/0004-6361:20052990.

D. S. Briggs. *High fidelity deconvolution of moderately resolved sources*. PhD thesis, New Mexico Institute of Mining and Technology, January 1995.

B. J. Burn. On the depolarization of discrete radio sources by Faraday dispersion. *Monthly Notices of the Royal Astronomical Society*, 133:67, January 1966. doi: 10.1093/mnras/133.1.67.

CASA Documentation. Deconvolution Algorithms, n.d. URL `https://casa.nrao.edu/casadocs/casa-5.1.1/synthesis-imaging/deconvolution-algorithms`. Accessed on 20/07/2022.

CASA Toolkit Reference Manual. Parameter weighting , n.d. URL `https://casa.nrao.edu/docs/casaref/imager.weight.html`. Accessed on 20/05/2022.

J. J. Condon and S. M. Ransom. *Essential Radio Astronomy*. Princeton University Press, 2016.

B. J. Geldzahler et al. High resolution observations of the quasar 3C 138. *Astronomy & Astrophysics*, 131:232–236, February 1984.

G. Heald. The Faraday rotation measure synthesis technique. *Proceedings of the International Astronomical Union*, 259:591–602, April 2009. doi: 10.1017/S1743921309031421.

J. A. Högbom. Aperture Synthesis with a Non-Regular Distribution of Interferometer Baselines. *Astronomy & Astrophysics*, 15:417, June 1974.

C. Horellou et al. The XXL Survey: XXXIV. Double irony in XXL-North. A tale of two radio galaxies in a supercluster at z = 0.14. *Astronomy & Astrophysics*, 620:A19, November 2018. doi: 10.1051/0004-6361/201832972.

M. Kierdorf et al. The magnetized disk-halo transition region of M 51. *Astronomy & Astrophysics*, 642:A118, October 2020. doi: 10.1051/0004-6361/202037847.

A. Kimball. VLA Data Reduction: Standard Calibration. *8th VLA Data Reduction Workshop*, 2021. URL `https://science.nrao.edu/science/meetings/2021/`

vla-data-reduction/presentations/calibration_tutorial_6.1.2.7.pdf. Accessed on 20/07/2022.

E. Le Roux. Étude théorique du rayonnement synchrotron des radiosources. *Annales d'Astrophysique*, 24:71, February 1961.

A. Mioduszewski. Array Configuration, Synthesis Imaging in Radio Astronomy, 2010. URL http://www.hartrao.ac.za/synthesis_school/Miod_Array_Design.pdf. Accessed on 20/05/2021.

I. Montoya Arroyave. A giant radio galaxy in XXL-North. Master's thesis, Chalmers University of Technology, 2019.

NRAO Telescopes. Very Large Array, n.d. URL https://public.nrao.edu/telescopes/vla/. Accessed on 16/04/2021.

A. G. Pacholczyk. *Radio astrophysics. Nonthermal processes in galactic and extragalactic sources*. W. H. Freeman and Company, 1970.

R. A. Perley and B. J. Butler. INTEGRATED POLARIZATION PROPERTIES OF 3c48, 3c138, 3c147, AND 3c286. *The Astrophysical Journal Supplement Series*, 206(2):16, may 2013. doi: 10.1088/0067-0049/206/2/16. URL https://doi.org/10.1088/0067-0049/206/2/16.

R. A. Perley and B. J. Butler. An accurate flux density scale from 50 MHz to 50 GHz. *The Astrophysical Journal Supplement Series*, 230(1):7, may 2017. doi: 10.3847/1538-4365/aa6df9. URL https://doi.org/10.3847/1538-4365/aa6df9.

M. Pierre et al. The XXL Survey. I. Scientific motivations - XMM-Newton observing plan - Follow-up observations and simulation programme. *Astronomy & Astrophysics*, 592:A1, June 2016. doi: 10.1051/0004-6361/201526766.

M. Pierre et al. The XXL survey: First results and future. *Astronomische Nachrichten*, 338(334):334–341, March 2017. doi: 10.1002/asna.201713352.

U. Rau and T. J. Cornwell. A multi-scale multi-frequency deconvolution algorithm for synthesis imaging in radio interferometry. *Astronomy & Astrophysics*, 532: A71, August 2011. doi: 10.1051/0004-6361/201117104.

G. B. Rybicki and A. P. Lightman. *Radiative processes in astrophysics*. A Wiley-Interscience Publication, New York, 1979.

SIMBAD Astronomical Database. Cul 0155-109, n.d. URL http://simbad.u-strasbg.fr/simbad/sim-id?Ident=Cul+0155-109. Accessed on 20/05/2021.

V. Smolčić et al. The XXL Survey. XXIX. GMRT 610 MHz continuum observations. *Astronomy & Astrophysics*, 620:A14, December 2018. doi: 10.1051/0004-6361/201732336.

B. W. Sohn. Ricean bias correction in linear polarization observation. *Journal of Astronomy and Space Sciences*, 28:267–271, 12 2011. doi: 10.5140/JASS.2011.28.4.267.

A. R. Thompson and R. N. Bracewell. Interpolation and Fourier transformation of fringe visibilities. *The Astronomical Journal*, 79:11–24, January 1974. doi: 10.1086/111523.

A. R. Thompson, J. M. Moran, and J. Swenson, George W. *Interferometry and Synthesis in Radio Astronomy, 3rd Edition*. Springer, 2017. doi: 10.1007/978-3-319-44431-4.

VLA Calibrators. NRAO, List of VLA Calibrators, n.d. URL `https://science.nrao.edu/facilities/vla/observing/callist`. Accessed on 05/05/2021.

VLA Manuals. Resolution, n.d. URL `https://science.nrao.edu/facilities/vla/docs/manuals/oss/performance/resolution`. Accessed on 10/06/2021.

J. F. C. Wardle and P. P. Kronberg. The linear polarization of quasi-stellar radio sources at 3.71 and 11.1 centimeters. *The Astrophysical Journal*, 194:249, January 1974. doi: 10.1086/153240.

J. F. C. Wardle. Magnetic fields and polarization in AGN jets. In *European Physical Journal Web of Conferences*, volume 61 of *European Physical Journal Web of Conferences*, page 06001, December 2013. doi: 10.1051/epjconf/20136106001.

T. L. Wilson, K. Rohlfs, and S. Hüttemeister. *Tools of Radio Astronomy*. Springer-Verlag Berlin Heidelberg, 2013. doi: 10.1007/978-3-642-39950-3.

A

Appendix

A.1 Individual Spectral Windows Stokes I

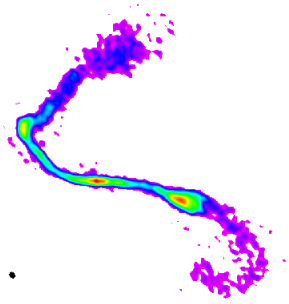

SPW 16

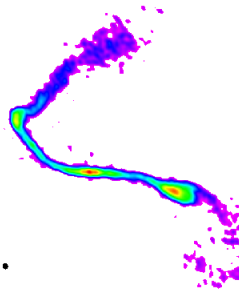

SPW 17

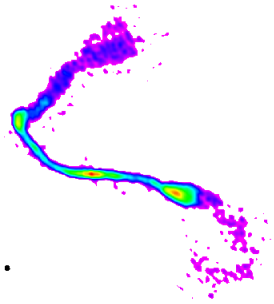

SPW 18

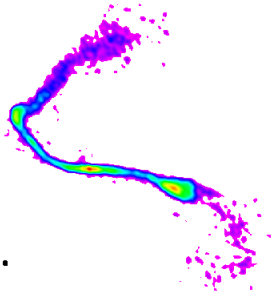

SPW 19

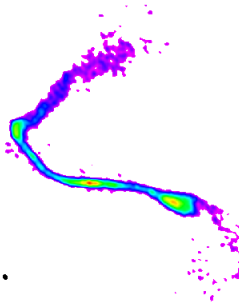

SPW 20

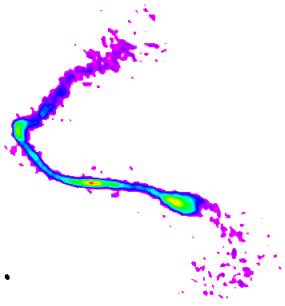

SPW 21

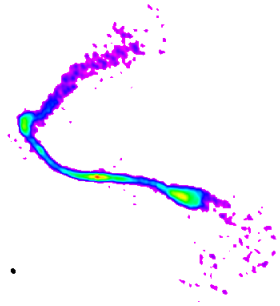

SPW 22

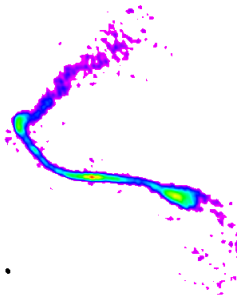

SPW 23

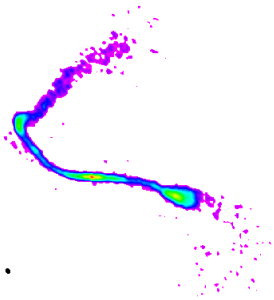

SPW 24

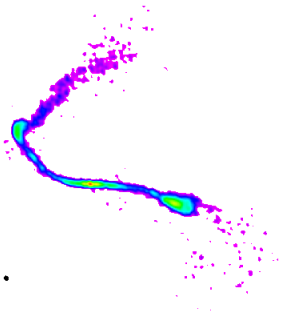

SPW 25

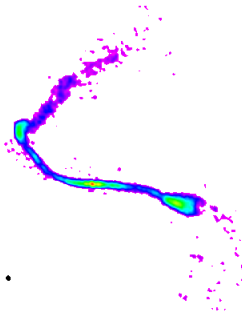

SPW 26

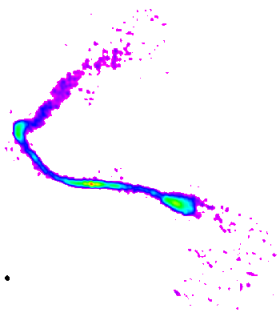

SPW 27

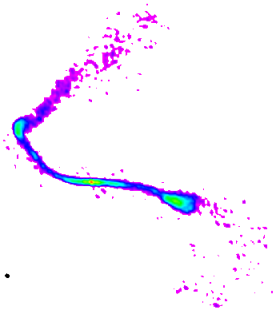

SPW 29

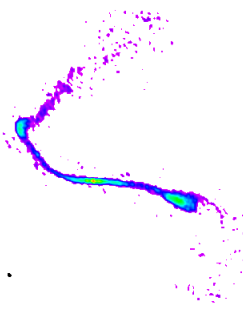

SPW 30

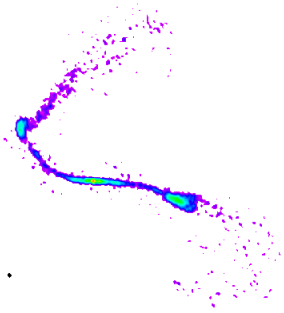

SPW 31

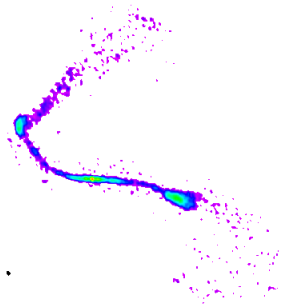

SPW 32

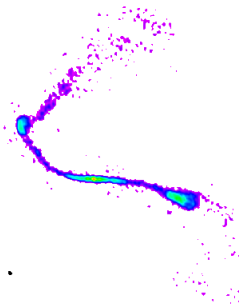

SPW 33

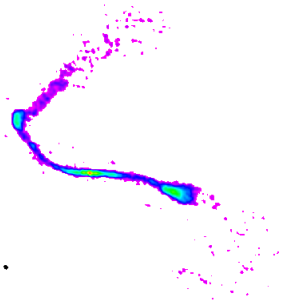

SPW 34

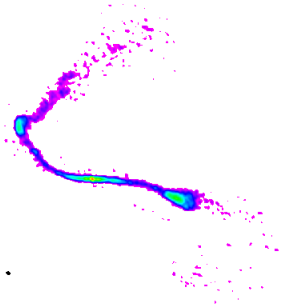

SPW 35

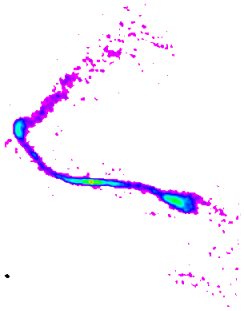

SPW 36

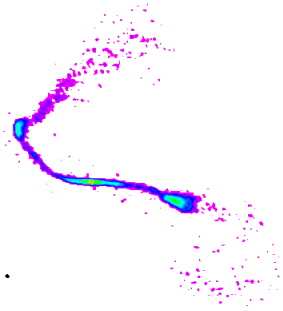

SPW 37

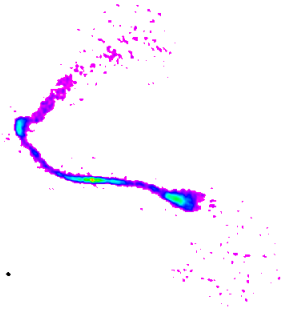

SPW 38

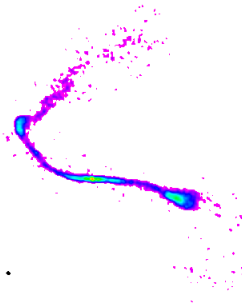

SPW 39

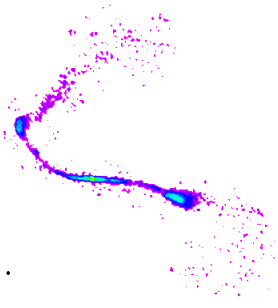

SPW 40

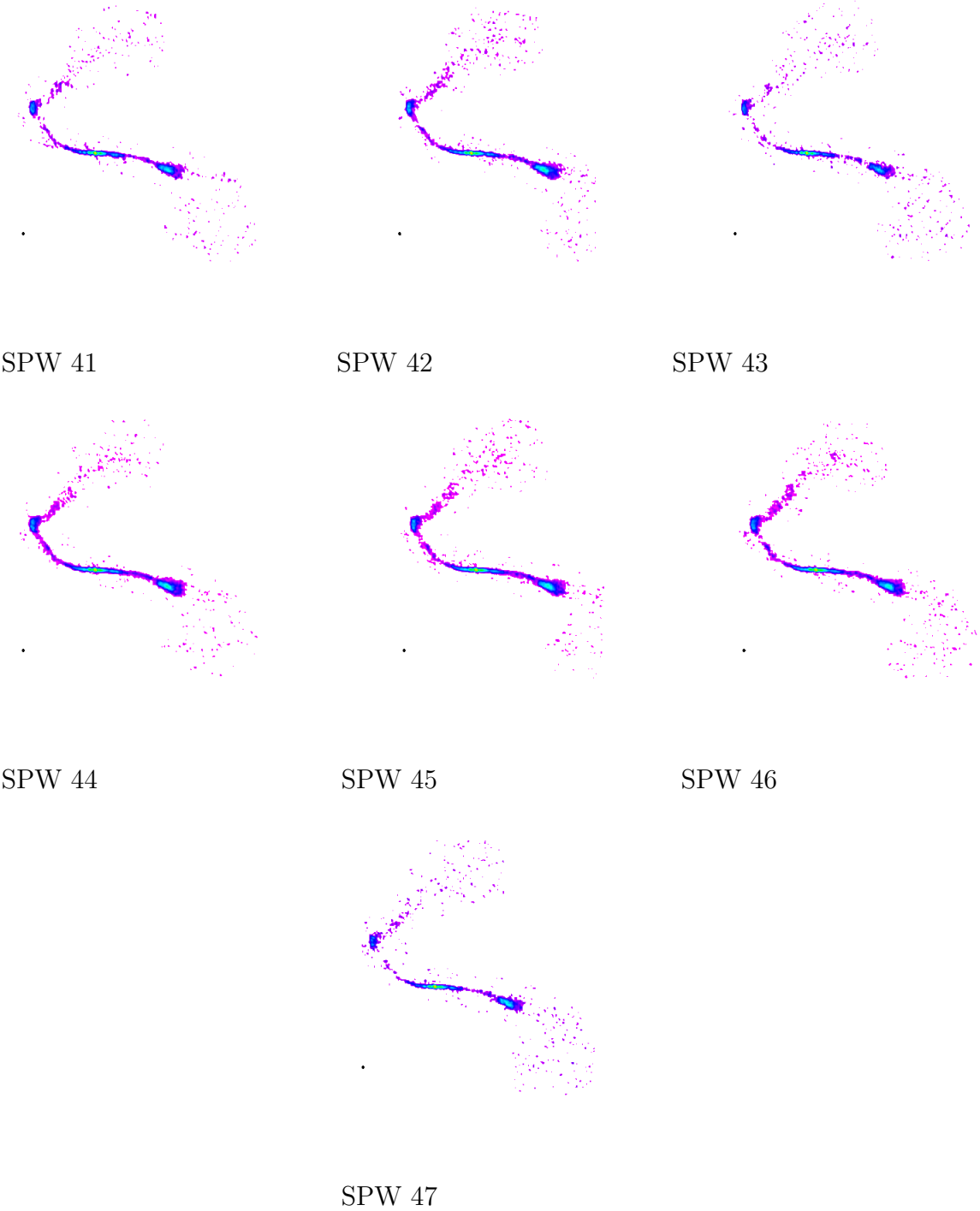

SPW 41 SPW 42 SPW 43

SPW 44 SPW 45 SPW 46

SPW 47

Figure A.1: Stokes I of individual spectral windows

SPW	ν_c (GHz)	$\Delta\nu$ (MHz)	Baseband
16	4.289	128.000	A1C1
17	4.417	128.000	A1C1
18	4.545	128.000	A1C1
19	4.673	128.000	A1C1
20	4.801	128.000	A1C1
21	4.929	128.000	A1C1
22	5.057	128.000	A1C1
23	5.185	128.000	A1C1
24	5.313	128.000	A1C1
25	5.441	128.000	A1C1
26	5.569	128.000	A1C1
27	5.697	128.000	A1C1
28	5.825	128.000	A1C1
29	5.953	128.000	A1C1
30	6.081	128.000	A1C1
31	6.209	128.000	A1C1
32	6.239	128.000	A2C2
33	6.367	128.000	A2C2
34	6.495	128.000	A2C2
35	6.623	128.000	A2C2
36	6.751	128.000	A2C2
37	6.879	128.000	A2C2
38	7.007	128.000	A2C2
39	7.135	128.000	A2C2
40	7.263	128.000	A2C2
41	7.391	128.000	A2C2
42	7.519	128.000	A2C2
43	7.647	128.000	A2C2
44	7.775	128.000	A2C2
45	7.903	128.000	A2C2
46	8.031	128.000	A2C2
47	8.159	128.000	A2C2

Table A.1: Spectral window data. Every SPW has LL, LR, RL, RR correlators, and 64 channels with a bandwidth of 2 MHz per channel.

A.2 VLA Observation Extra Information

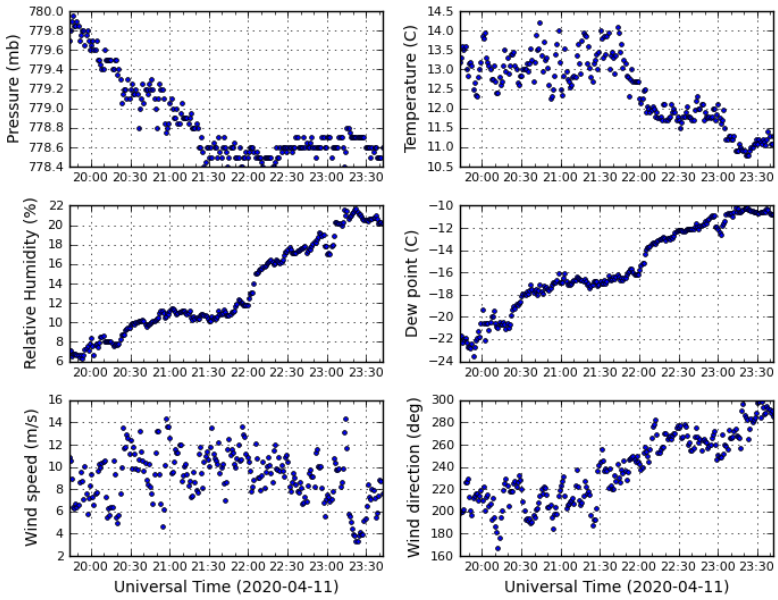

Figure A.2: Weather conditions at the VLA site during observation.

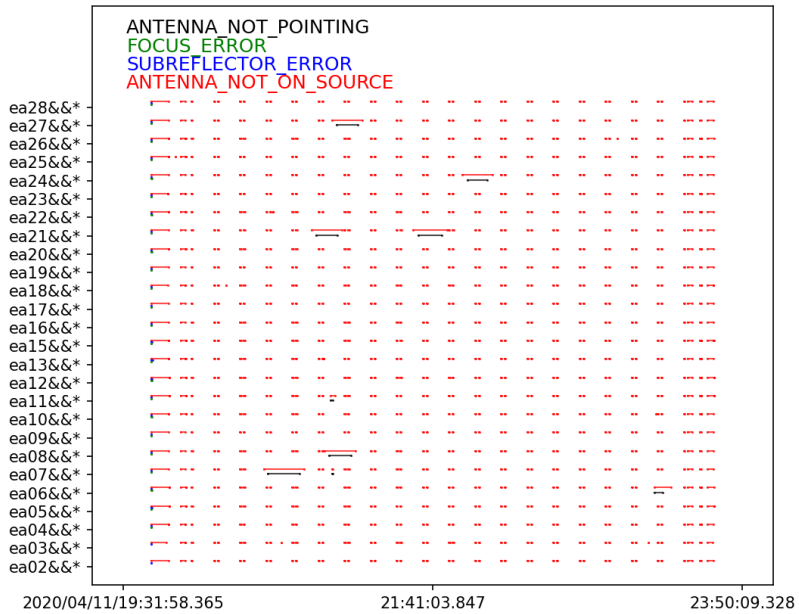

Figure A.3: Antenna pointings and errors.

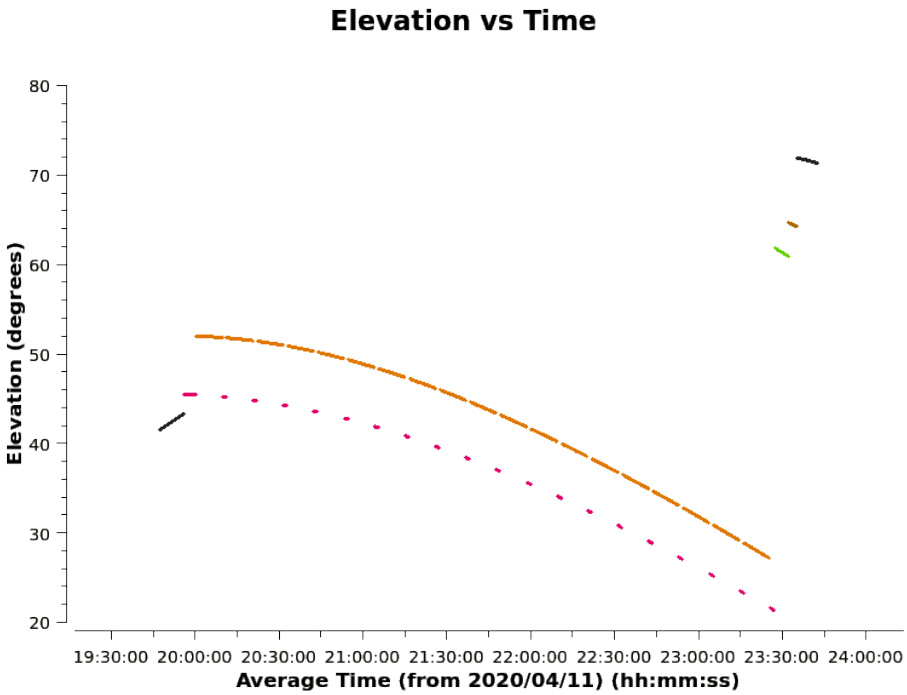

Figure A.4: Source elevation over time. Colored by scan target, Double Irony in orange.

DEPARTMENT OF SOME SUBJECT OR TECHNOLOGY
CHALMERS UNIVERSITY OF TECHNOLOGY
Gothenburg, Sweden
www.chalmers.se

CHALMERS
UNIVERSITY OF TECHNOLOGY